Engineering Structures 261 (2022) 114213

Contents lists available at ScienceDirect

Engineering Structures

journal homepage: www.elsevier.com/locate/engstruct

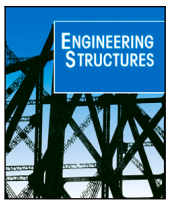

Accurate thermal-induced structural failure analysis under incompressible conditions

Carlos A. Moreira *, Gabriel B. Barbat, Miguel Cervera, Michele Chiumenti

International Center for Numerical Methods in Engineering (CIMNE), Technical University of Catalonia, Edificio C1, Campus Norte, Gran Capitán s/n, 08034 Barcelona, Spain

A B S T R A C T

In this work, the performance of the mixed 3-field *displacement/deviatoric-strain/pressure* ($\mathbf{u}/\mathbf{e}/p$) finite element is examined for nonlinear thermo-mechanical structural applications under incompressible behavior. The proposed FE model increases the solution accuracy in terms of strains and stresses, guaranteeing mesh-objective results in nonlinear analyses. Structural failure is modelled with J2-plasticity and J2-damage constitutive laws, introducing the isochoric behavior, typical of metals, in the material response. The solution of the coupled thermal and mechanical problems follows a staggered scheme and temperature dependent material properties are introduced to study the effect of the thermal coupling in the mechanical problem. This FE approach is applicable with any interpolation basis: triangles, quadrilaterals, tetrahedras, hexahedras and prisms.

A set of numerical benchmark problems is proposed to examine the influence of the enhanced accuracy of the proposed model in thermally-induced structural failure analyses in incompressible conditions. The study includes the comparison of the $\mathbf{u}/\mathbf{e}/p$ and $\mathbf{u}/p$ FE formulations, where the effect of the thermal coupling in the problem is investigated. The superior performance of the 3-field formulation with regard to the evaluation of collapse mechanisms, failure loads, mechanical dissipation and numerical stability in incompressible situations is shown.

1. Introduction

Isochoric behavior in solid mechanics can be found in situations with incompressible elasticity, such as rubber-like materials, or undrained saturated porous media; also, in nonlinear constitutive laws with isochoric flow, such as plasticity models using the Von Mises yield criterion typical for metals. In the latter case, the standard displacement-based formulation [1] fails to solve these incompressible situations, resulting in an almost completely locked solution, due to numerical difficulties caused by the volumetric constraints and spurious pressure oscillations [2–4].

To avoid or reduce the volumetric locking in these situations, several numerical strategies have been proposed in the literature. These are based on the use of mixed formulations [5–11], enhanced assumed strains methods [3,4,12–14], nodal pressure and strain averaging [15–19]; and reduced and selective integration [20–22]. Within the mixed approaches, the displacement/pressure ($\mathbf{u}/p$) FE has become a widespread method to solve incompressibility both in solid and fluid mechanics.

Recently, the authors have proposed the use of the mixed stress/displacement ($\boldsymbol{\sigma}/\mathbf{u}$) and strain/displacement ($\boldsymbol{\varepsilon}/\mathbf{u}$) finite element formulations to increase the accuracy of the computed solution in terms of stresses and strains [23–32]. This increase in the precision of the calculations has proven to be crucial to obtain mesh objective results in structural failure problems [24,28,29]. In nonlinear applications, the $\boldsymbol{\varepsilon}/\mathbf{u}$ FE is preferred over the $\boldsymbol{\sigma}/\mathbf{u}$ because it allows to readily implement and adopt the constitutive laws usually considered in solid mechanics, which are defined in strain-driven format.

In view of this, the 3-field displacements/deviatoric-stress/pressure $\mathbf{u}/\mathbf{s}/p$ and the displacement/deviatoric-strain/pressure $\mathbf{u}/\mathbf{e}/p$ FEs have been proposed to address incompressible problems with enhanced accuracy compared to the mixed displacement/pressure $\mathbf{u}/p$ FEs commonly adopted in isochoric problems [33–36]. These three methods require the constitutive equation split into its volumetric and deviatoric components.

Alternatively, the use of an $\bar{\varepsilon}$/B-bar method has been proposed, showing a better accuracy with respect to the standard B-bar approach also commonly adopted to solve nearly incompressible problems [10, 20–22]. These strategies present the advantage of not requiring the split of the constitutive equation in volumetric and deviatoric parts. Notwithstanding, this approach is unfit for the elastic incompressible limit ($\nu = 0.5$) and can be used only in the near incompressible limit. Also, they present the limitation of being restricted to quadrilaterals and hexahedral elements.

* Corresponding author.
E-mail addresses: carlos.augusto.moreira.filho@upc.edu (C.A. Moreira), gabriel.barbat@upc.edu (G.B. Barbat), miguel.cervera@upc.edu (M. Cervera), michele.chiumenti@upc.edu (M. Chiumenti).

https://doi.org/10.1016/j.engstruct.2022.114213
Received 20 December 2021; Received in revised form 18 March 2022; Accepted 27 March 2022
Available online 30 April 2022

Table 1
FE and their applicability.

	Standard ($\mathbf{u}$)	B-bar	$\mathbf{u}/p$	σ/u	$\epsilon/\mathbf{u}$	$\bar{\epsilon}$/B-bar	$\mathbf{u}/s/p$	$\mathbf{u}/\mathbf{e}/p$
References	[1]	[20–22]	[5–11]	[28]	[23–27,29–31]	[10]	[34]	[33,35]
Incompressibility	✘	✓*	✓	✘	✘	✓*	✓	✓
Strain-driven constitutive laws	✓	✓	✓	✘	✓	✓	✘	✓
Avoids the split of constitutive equations	✓	✓	✘	✓	✓	✓	✘	✘
Higher stress/strain accuracy	✘	✘	✘	✓	✓	✓	✓	✓
General interpolation basis (triangles, quadrilaterals, tetrahedras, hexahedras, prisms)	✓	✘	✓	✓	✓	✘	✓	✓

Table 1 summarizes the advantages and disadvantages of these alternative formulations. The superscript (*) in the B-bar and $\bar{\epsilon}$/B-bar methods indicates that they are not apt for fully incompressible problems and are used for near incompressibility only.

In our previous work [35] it was shown that, when considering incompressibility, the mixed displacement/deviatoric-strain/pressure $\mathbf{u}/\mathbf{e}/p$ formulation allows for a better evaluation of stresses, strains and mechanical dissipation than the mixed displacement/pressure $\mathbf{u}/p$ element and that a spurious overestimation of the mechanical dissipation in nonlinear analyses takes place with the $\mathbf{u}/p$ FE.

Mixed finite elements have been extensively used to solve problems involving softening behavior in damage and plasticity, strain localization and size-effect [27–29,32,37–41], but few studies, so far, have been conducted considering non-isothermal behavior [42–45].

Saloustros et al. (2021) [10] detail the advantages of using mixed solid elements to address typical plate, beam and shell problems; among them: this approach does not require additional kinematical hypotheses (planar sections; shear stress and warping through the thickness); does not pose compatibility problems between different elements used by the structural model; can easily accommodate construction details (e.g., web-perforated steel beams, layered elements, element-stiffeners); does not require rotational degrees of freedom and awkward boundary condition alternatives (e.g., “soft” and “hard” supports). In the specific case of thermal loading, no additional assumptions need to be made about the through thickness temperature distribution.

Alternatively, the Carrera Unified Formulation (CUF) [46] has been applied to solve different multifield problems in multilayered structures using beam, plates and shell elements. The CUF has been used with thermal loads [47], thermo-elastic coupling [48,49], piezoelectric structures [50,51] and a complete multifield formulation has been proposed [52,53].

The interest in solving coupled thermo-mechanical problems arises from engineering applications where temperature-dependency of the mechanical properties is relevant as, for instance, on the fire analysis of structures, manufacturing processes (casting, welding, additive manufacturing, etc.), aerospace industry, turbines and high-speed civil transport industry [54]. Specifically, in structural failure problems, the presence of an external heat source and/or the mechanical dissipation that takes place during the process may produce an increase in the temperature field that significantly influences the observed nonlinear behavior of the material.

For these reasons, this work focuses on the accurate analysis of thermally-coupled structural failure under isochoric conditions. The computation of the coupled thermal and mechanical problems is made following a staggered approach. The mixed $\mathbf{u}/\mathbf{e}/p$ FE formulation is employed to solve the mechanical problem, with the aim of increasing the accuracy of the computed stresses, strains and mechanical dissipation and to obtain mesh-objective results. Structural failure is modelled using J2-damage and J2-plasticity constitutive laws, introducing an incompressible behavior in the material nonlinear response. The thermal problem is solved using an implicit Euler method and temperature-dependent material properties are considered in the analysis. A comparison of the performance of the 3-field formulation with the $\mathbf{u}/p$ element is introduced to assess the advantages of the proposed model.

The objectives of this paper are: (1) to extend the mixed $\mathbf{u}/\mathbf{e}/p$ formulation to address the incompressible limit and isochoric constitutive laws in thermo-mechanical applications; (2) to investigate the influence of temperature-dependent parameters in thermo-mechanical failure; (3) to assess the enhanced accuracy of the 3-field ($\mathbf{u}/\mathbf{e}/p$) over the mixed $\mathbf{u}/p$ in thermo-mechanical analyses.

Therefore, the paper is organized as follows. Section 2 addresses the mixed $\mathbf{u}/\mathbf{e}/p$ strong and weak forms, as well as the resulting FE formulation. In Section 3 the coupling between the thermal and mechanical problems is introduced. In Section 4 the constitutive models adopted in the numerical examples, isotropic J2-damage and J2-plasticity, are summarized. In Section 5 several numerical simulations are presented to compare the performance and accuracy of the 3-field formulation with respect to the $\mathbf{u}/p$ FE in thermo-mechanical problems. Finally, Section 6 presents the concluding remarks.

2. Mixed 3-field ($\mathbf{u}/\mathbf{e}/p$) mechanical problem

2.1. Volumetric/deviatoric split

Using Voigt’s notation, in 3D, the displacement $\mathbf{u} = (u, v, w)^T$ is a vector of 3 components and the stress $\boldsymbol{\sigma} = (\sigma_x, \sigma_y, \sigma_z, \tau_{xy}, \tau_{yz}, \tau_{xz})^T$ and the strain $\boldsymbol{\epsilon} = (\epsilon_x, \epsilon_y, \epsilon_z, \epsilon_{xy}, \epsilon_{yz}, \epsilon_{xz})^T$ are vectors of 6 components.

The constitutive equation relates the stress vector σ and the strain vector $\boldsymbol{\epsilon}$

$$\boldsymbol{\sigma} = \mathbf{C}\boldsymbol{\epsilon} \tag{1}$$

where $\mathbf{C}$ is the fourth-order secant constitutive tensor expressed in Voigt’s notation as a 6×6 matrix. In this work, the nonlinear mechanical behavior is introduced through the adoption of the J2-damage and J2-plasticity constitutive laws, presented in Section 4. These establish the nonlinear relation between stresses and strains followed by the material and define the corresponding secant constitutive matrix $\mathbf{C}$.

Herein, the volumetric/deviatoric split of the stresses and strains is introduced, respectively as:

$$\boldsymbol{\sigma} = p\mathbf{I} + \mathbf{s} \tag{2}$$

$$\boldsymbol{\epsilon} = \frac{1}{3}e_{vol}\mathbf{I} + \mathbf{e} \tag{3}$$

where $\mathbf{I} = (1, 1, 1, 0, 0, 0)^T$ is the second-order identity tensor in Voigt’s notation, p is the pressure, which is a scalar, and $\mathbf{s}$ is the deviatoric-stress vector

$$p = \frac{1}{3}(\sigma_x + \sigma_y + \sigma_z) \tag{4}$$

$$\mathbf{s} = (\sigma_x - p, \sigma_y - p, \sigma_z - p, \tau_{xy}, \tau_{yz}, \tau_{xz})^T \tag{5}$$

also, e_{vol} is the volumetric strain (scalar), and $\mathbf{e}$ is the deviatoric-strain vector, defined as

$$e_{vol} = (\epsilon_x + \epsilon_y + \epsilon_z) = \mathbf{G}^T\mathbf{u} \tag{6}$$

$$\mathbf{e} = (\varepsilon_x - \frac{1}{3}e_{vol}, \varepsilon_y - \frac{1}{3}e_{vol}, \varepsilon_z - \frac{1}{3}e_{vol}, \varepsilon_{xy}, \varepsilon_{yz}, \varepsilon_{xz})^T \tag{7}$$

e_{vol} can be computed as the divergence of the displacements $\mathbf{u}$ where $\mathbf{G} = (\partial_x, \partial_y, \partial_z)^T$ is the gradient operator and $\mathbf{G}^T$ is the adjoint divergence operator.

The volumetric/deviatoric split is also applied to the constitutive relationship:

$$p = C^{vol} e_{vol} \tag{8}$$

$$\mathbf{s} = \mathbf{C}^{dev}\mathbf{e} \tag{9}$$

where C^{vol} is defined as $C^{vol} = \frac{1}{9}\mathbf{I}^T\mathbf{C}\mathbf{I}$ and $\mathbf{C}^{dev}$ is the deviatoric secant constitutive matrix.

Note that

$$\mathbf{s} = \mathbf{C}^{dev}\boldsymbol{\varepsilon} \tag{10}$$

Let $\mathbf{J}$ be the fourth-order identity tensor, expressed following Voigt's notation as a 6×6 identity matrix

$$\mathbf{J} = \begin{bmatrix} 1 & 0 & 0 & 0 & 0 & 0 \\ 0 & 1 & 0 & 0 & 0 & 0 \\ 0 & 0 & 1 & 0 & 0 & 0 \\ 0 & 0 & 0 & 1 & 0 & 0 \\ 0 & 0 & 0 & 0 & 1 & 0 \\ 0 & 0 & 0 & 0 & 0 & 1 \end{bmatrix} \tag{11}$$

and the volumetric and deviatoric fourth-order operators, $\mathbf{V}$ and $\mathbf{Y}$, respectively, are introduced in Voigt's notation as

$$\mathbf{V} = \frac{1}{3}\mathbf{I}\mathbf{I}^T = \frac{1}{3}\begin{bmatrix} 1 & 1 & 1 & 0 & 0 & 0 \\ 1 & 1 & 1 & 0 & 0 & 0 \\ 1 & 1 & 1 & 0 & 0 & 0 \\ 0 & 0 & 0 & 0 & 0 & 0 \\ 0 & 0 & 0 & 0 & 0 & 0 \\ 0 & 0 & 0 & 0 & 0 & 0 \end{bmatrix} \tag{12}$$

$$\mathbf{Y} = \mathbf{J} - \mathbf{V} = \frac{1}{3}\begin{bmatrix} 2 & -1 & -1 & 0 & 0 & 0 \\ -1 & 2 & -1 & 0 & 0 & 0 \\ -1 & -1 & 2 & 0 & 0 & 0 \\ 0 & 0 & 0 & 3 & 0 & 0 \\ 0 & 0 & 0 & 0 & 3 & 0 \\ 0 & 0 & 0 & 0 & 0 & 3 \end{bmatrix} \tag{13}$$

For the case of isotropic materials, C^{vol} and $\mathbf{C}^{dev}$ in Eqs. (8) and (9) can be written as

$$C^{vol} = K \tag{14}$$

$$\mathbf{C}^{dev} = \mathbf{Y}\mathbf{C} = 2G\mathbf{Y} \tag{15}$$

where K is the secant bulk modulus and G is the secant shear modulus.

This leads to the following constitutive relationships:

$$p = Ke_{vol} \tag{16}$$

$$\mathbf{s} = 2G\mathbf{e} \tag{17}$$

2.2. Strong form

The strong form of the nonlinear solid mechanics problem is written in terms of the displacement $\mathbf{u}$, deviatoric-strain $\mathbf{e}$, and pressure p fields. The displacement $\mathbf{u}$ and the total strains $\boldsymbol{\varepsilon}$ are related through the compatibility equation

$$\boldsymbol{\varepsilon} = \mathbf{S}\mathbf{u} \tag{18}$$

where $\mathbf{S}$ is the differential symmetric gradient operator

$$\mathbf{S} = \begin{bmatrix} \partial_x & 0 & 0 & \partial_y & 0 & \partial_z \\ 0 & \partial_y & 0 & \partial_x & \partial_z & 0 \\ 0 & 0 & \partial_z & 0 & \partial_y & \partial_x \end{bmatrix}^T \tag{19}$$

Equilibrium between the stress vector $\boldsymbol{\sigma}$ and the body forces $\mathbf{f} = (f_x, f_y, f_z)^T$ is defined by the Cauchy equation

$$\mathbf{S}^T\boldsymbol{\sigma} + \mathbf{f} = \mathbf{0} \tag{20}$$

where $\mathbf{S}^T$ is the differential divergence operator, adjoint to the $\mathbf{S}$ in Eq. (18).

Introducing the split of the strains, Eqs. (3) and (6), in Eq. (18), leads to

$$\mathbf{e} = \mathbf{S}\mathbf{u} - \frac{1}{3}\mathbf{I}\underbrace{(\mathbf{G}^T\mathbf{u})}_{e_{vol}} = \mathbf{W}\mathbf{u} \tag{21}$$

where $\mathbf{W}$ is the operator defined as

$$\mathbf{W} = \mathbf{S} - \frac{1}{3}\mathbf{I}\mathbf{G}^T = \frac{1}{3}\begin{bmatrix} 2\partial_x & -\partial_x & -\partial_x & 3\partial_y & 0 & 3\partial_z \\ -\partial_y & 2\partial_y & -\partial_y & 3\partial_x & 3\partial_z & 0 \\ -\partial_z & -\partial_z & 2\partial_z & 0 & 3\partial_y & 3\partial_x \end{bmatrix}^T \tag{22}$$

Note that $\mathbf{W} = \mathbf{Y}\mathbf{S}$.

Next, introducing Eqs. (2) and (9) in Eq. (20), where the identity $\mathbf{S}^T\mathbf{I} = \mathbf{G}$ is used, and Eq. (6) in Eq. (8), the continuous strong form of the mixed $\mathbf{u}/\mathbf{e}/p$ formulation is

$$\begin{aligned} \mathbf{S}^T(\mathbf{C}^{dev}\mathbf{e}) + \mathbf{G}p + \mathbf{f} &= \mathbf{0} \\ \mathbf{W}\mathbf{u} - \mathbf{e} &= \mathbf{0} \\ \mathbf{G}^T\mathbf{u} - \frac{p}{C^{vol}} &= 0 \end{aligned} \tag{23}$$

together with the prescribed mechanical boundary conditions. The boundary Γ can be split according to the Dirichlet and Newman conditions imposed, respectively as Γ_u and Γ_t, such that $\Gamma = \Gamma_u \cup \Gamma_t$ and $\Gamma_u \cap \Gamma_t = \varnothing$.

It is assumed herein that the prescribed displacements vanish on the boundary Γ_u

$$\mathbf{u} = \mathbf{0} \text{ in } \Gamma_u \tag{24}$$

In addition, the prescribed traction on the boundary Γ_t are

$$\mathbf{t} = \bar{\mathbf{t}} \text{ in } \Gamma_t \tag{25}$$

2.3. Weak form

The variational form of the problem in Eqs. (23) is then obtained as follows.

Firstly, Eq. (23)*a* is premultiplied by an arbitrary virtual displacement $\delta\mathbf{u}$ and integrated over the spatial domain:

$$\int_\Omega \delta\mathbf{u}^T[\mathbf{S}^T(\mathbf{C}^{dev}\mathbf{e})]d\Omega + \int_\Omega \delta\mathbf{u}^T[\mathbf{G}p]d\Omega + \int_\Omega \delta\mathbf{u}^T\mathbf{f}\,d\Omega = \mathbf{0} \qquad \forall\delta\mathbf{u} \tag{26}$$

The virtual displacement $\delta\mathbf{u}$ also conforms with the boundary conditions, so that $\delta\mathbf{u} = \mathbf{0}$ in Γ_u. Then, the Divergence Theorem is applied to the first and second terms of Eq. (26) and the boundary term is split $\Gamma = \Gamma_u \cup \Gamma_t$. The Dirichlet boundary terms vanish ($\delta\mathbf{u} = \mathbf{0}$) and, considering that $\mathbf{S}^T\mathbf{I} = \mathbf{G}$, the variational form of Eq. (26) becomes

$$\begin{aligned} \int_\Omega (\mathbf{S}\delta\mathbf{u})^T(\mathbf{C}^{dev}\mathbf{e})d\Omega + \int_\Omega (\mathbf{S}\delta\mathbf{u})^T(p\mathbf{I})d\Omega &= \int_\Omega \delta\mathbf{u}^T\mathbf{f}\,d\Omega + \int_{\Gamma_t} \delta\mathbf{u}^T\bar{\mathbf{t}}\,d\Gamma \\ &= W(\delta\mathbf{u}) \quad \forall\delta\mathbf{u} \end{aligned} \tag{27}$$

Eq. (27) is equivalent to the Principle of Virtual Work, as the right hand side term, noted $W(\delta\mathbf{u})$, is the virtual work done by the traction $\bar{\mathbf{t}}$ and body forces $\mathbf{f}$ while the left hand side constitutes the virtual work of the internal forces.

Secondly, Eq. (23)*b* is premultiplied by $\mathbf{C}^{dev}$ to obtain a symmetric problem and then premultiplied by an arbitrary virtual deviatoric-strain vector $\delta\mathbf{e}$ and integrated over the spatial domain

$$\int_\Omega \delta\mathbf{e}^T[\mathbf{C}^{dev}(\underbrace{\mathbf{Y}\mathbf{S}}_{=\mathbf{W}}\mathbf{u})]d\Omega - \int_\Omega \delta\mathbf{e}^T(\mathbf{C}^{dev}\mathbf{e})d\Omega = \mathbf{0} \qquad \forall\delta\mathbf{e} \tag{28}$$

Note that $\mathbf{C}^{dev}\mathbf{Y} = \mathbf{C}^{dev}$.

Thirdly, Eq. (23)*c* is premultiplied by an arbitrary virtual pressure vector δp and integrated over the spatial domain

$$\int_\Omega \delta p^T(\mathbf{G}^T\mathbf{u})d\Omega - \int_\Omega \delta p^T \frac{p}{C^{vol}}d\Omega = 0 \qquad \forall \delta p \tag{29}$$

The resulting variational form of the 3-field formulation is:

$$\begin{array}{ll} \int_\Omega (\mathbf{S}\delta\mathbf{u})^T(\mathbf{C}^{dev}\mathbf{e})d\Omega + \int_\Omega (\mathbf{S}\delta\mathbf{u})^T(p\mathbf{I})d\Omega = W(\delta\mathbf{u}) & \forall \delta\mathbf{u} \\ \int_\Omega \delta\mathbf{e}^T[\mathbf{C}^{dev}(\mathbf{S}\mathbf{u})]d\Omega - \int_\Omega \delta\mathbf{e}^T(\mathbf{C}^{dev}\mathbf{e})d\Omega = \mathbf{0} & \forall \delta\mathbf{e} \\ \int_\Omega \delta p^T(\mathbf{G}^T\mathbf{u})d\Omega - \int_\Omega \delta p^T \frac{p}{C^{vol}}d\Omega = 0 & \forall \delta p \end{array} \tag{30}$$

The solution to the mixed problem is: find the unknowns $\mathbf{u}$, $\mathbf{e}$ and p that verify the system of Eqs. (30) and comply with the boundary condition $\mathbf{u} = \mathbf{0}$ on Γ_u given the arbitrary virtual displacement $\delta\mathbf{u}$, which also vanishes on Γ_u and the arbitrary virtual deviatoric-strain and pressure $\delta\mathbf{e}$ and δp, respectively.

2.4. FE approximation

The continuous domain of the problem is discretized in a FE partition such that $\Omega = \cup\Omega_e$, and discrete FE approximations of the displacements $\mathbf{u}$, the deviatoric-strains $\mathbf{e}$ and the pressure p are taken, such that

$$\begin{aligned} \mathbf{u} &\doteq \hat{\mathbf{u}} = \mathbf{N}_u\mathbf{U} \\ \mathbf{e} &\doteq \hat{\mathbf{e}} = \mathbf{N}_e\mathbf{E} \\ p &\doteq \hat{p} = \mathbf{N}_p\mathbf{P} \end{aligned} \tag{31}$$

where $\mathbf{U}$, $\mathbf{E}$ and $\mathbf{P}$ are vectors comprising the values of the displacements, deviatoric-strains and pressures at the nodes of the finite element mesh. $\mathbf{N}_u$, $\mathbf{N}_e$ and $\mathbf{N}_p$ are the matrices containing the interpolation functions adopted in the FE approximation.

In the Galerkin method, the same approximation is taken for the discrete virtual displacements, virtual deviatoric-strains and virtual pressure, so that

$$\begin{aligned} \delta\mathbf{u} &\doteq \delta\hat{\mathbf{u}} = \mathbf{N}_u\delta\mathbf{U} \\ \delta\mathbf{e} &\doteq \delta\hat{\mathbf{e}} = \mathbf{N}_e\delta\mathbf{E} \\ \delta p &\doteq \delta\hat{p} = \mathbf{N}_p\delta\mathbf{P} \end{aligned} \tag{32}$$

Introducing these approximations, the system of Eqs. (30) becomes:

$$\begin{array}{ll} \int_\Omega \underbrace{(\mathbf{S}\mathbf{N}_u\delta\mathbf{U})^T}_{=\delta\mathbf{U}^T\mathbf{B}_u^T}(\mathbf{C}^{dev}\mathbf{N}_e\mathbf{E})d\Omega + \int_\Omega (\mathbf{S}\mathbf{N}_u\delta\mathbf{U})^T(\mathbf{N}_p\mathbf{P}\mathbf{I})d\Omega = \hat{W}(\delta\mathbf{U}) & \forall\delta\mathbf{U} \\ \int_\Omega \delta\mathbf{E}^T\mathbf{N}_e^T[\mathbf{C}^{dev}\underbrace{(\mathbf{S}\mathbf{N}_u\mathbf{U})}_{=\mathbf{B}_u\mathbf{U}}]d\Omega - \int_\Omega \delta\mathbf{E}^T\mathbf{N}_e^T(\mathbf{C}^{dev}\mathbf{N}_e\mathbf{E})d\Omega = \mathbf{0} & \forall\delta\mathbf{E} \\ \int_\Omega \delta\mathbf{P}^T\mathbf{N}_p^T(\mathbf{G}^T\mathbf{N}_u\mathbf{U})d\Omega - \int_\Omega^T \delta\mathbf{P}^T\mathbf{N}_p^T\frac{\mathbf{N}_p\mathbf{P}}{C^{vol}}d\Omega = 0 & \forall\delta\mathbf{P} \end{array} \tag{33}$$

where $\mathbf{B}_u = \mathbf{S}\mathbf{N}_u$ is the discrete strain–displacement matrix.

In Eq. (33)*a* $\hat{W}(\delta\mathbf{U})$ is the work done by the traction $\bar{\mathbf{t}}$ and body forces $\mathbf{f}$ defined as

$$\hat{W}(\delta\mathbf{U}) = \int_\Omega \delta\mathbf{U}^T\mathbf{N}_u^T\mathbf{f}d\Omega + \int_{\Gamma_t}\delta\mathbf{U}^T\mathbf{N}_u^T\bar{\mathbf{t}}d\Gamma \tag{34}$$

Note that the equality $\mathbf{G} = \mathbf{S}^T\mathbf{I}$ can be used again in the second term in Eq. (33)*a*

$$\int_\Omega (\mathbf{S}\mathbf{N}_u\delta\mathbf{U})^T(\mathbf{N}_p\mathbf{P}\mathbf{I})d\Omega = \int_\Omega \delta\mathbf{U}^T\mathbf{N}_u^T\mathbf{S}^T\mathbf{I}\mathbf{N}_p\mathbf{P}d\Omega = \int_\Omega \delta\mathbf{U}^T\mathbf{N}_u^T\mathbf{G}\mathbf{N}_p\mathbf{P}d\Omega \tag{35}$$

This shows that the resulting problem is symmetric.

The virtual displacement $\delta\mathbf{U}$, virtual deviatoric-strain $\delta\mathbf{E}$ and virtual pressure $\delta\mathbf{P}$ are arbitrary nodal vectors. Therefore, the system of Eqs. (33) can be written in matrix form as

$$\begin{bmatrix} \mathbf{0} & \mathbf{K}_{UE} & \mathbf{K}_{UP} \\ (\mathbf{K}_{UE})^T & -\mathbf{M}_{EE} & \mathbf{0} \\ (\mathbf{K}_{UP})^T & \mathbf{0} & -\mathbf{M}_{PP} \end{bmatrix}\begin{bmatrix} \mathbf{U} \\ \mathbf{E} \\ \mathbf{P} \end{bmatrix} = \begin{bmatrix} \mathbf{F} \\ \mathbf{0} \\ \mathbf{0} \end{bmatrix} \tag{36}$$

where $[\mathbf{U}\,\mathbf{E}\,\mathbf{P}]^T$ is the array of nodal values of displacements, deviatoric-strains and pressure and

$$\mathbf{M}_{EE} = \int_\Omega \mathbf{N}_e^T\mathbf{C}^{dev}\mathbf{N}_e d\Omega \tag{37}$$

$$\mathbf{M}_{PP} = \int_\Omega \mathbf{N}_p^T\frac{1}{C^{vol}}\mathbf{N}_p d\Omega \tag{38}$$

$$\mathbf{K}_{UE} = \int_\Omega \mathbf{B}_u^T\mathbf{C}^{dev}\mathbf{N}_e d\Omega \tag{39}$$

$$\mathbf{K}_{UP} = \int_\Omega \mathbf{N}_u^T\mathbf{G}\mathbf{N}_p d\Omega \tag{40}$$

and

$$\mathbf{F} = \int_\Omega \mathbf{N}_u^T\mathbf{f}d\Omega + \int_{\Gamma_t}\mathbf{N}_u^T\bar{\mathbf{t}}d\Gamma \tag{41}$$

2.5. Variational multi-scale stabilization

A crucial issue for mixed methods is stability. In order to ensure this, the mixed interpolation adopted needs to satisfy the Inf–Sup condition. However, stable combinations of interpolation spaces are problem dependent, difficult to formulate and, often, rather exotic [6,55–58].

A common strategy when using mixed FEs is to adopt equal order interpolation functions for all the proposed fields. This approach is preferred because it is far simpler to formulate and implement. However, equal order interpolation does not comply with the Inf–Sup condition [59,60] and requires the use of a stabilization method. Techniques based on the Variational Multi-Scale method (VMS) [61–63] have been used to this end. They consist on the numerical enrichment of the FE fields adding a fine scale refinement to the FE solution, which provides the discrete problem with the necessary stability. Within the VMS approach, Codina introduced the Orthogonal Subgrid-Scales (OSS) in which the fine scales are chosen orthogonal to the FE space [64–66].

The VMS technique has been successfully applied to stabilize the following mixed formulations using equal order linear approximations for all fields: displacement/pressure ($\mathbf{u}/p$); stress/displacement ($\boldsymbol{\sigma}/\mathbf{u}$); strain/displacement ($\boldsymbol{\varepsilon}/\mathbf{u}$); displacement/deviatoric-stress/pressure ($\mathbf{u}/\mathbf{s}/p$); as well as the displacement/deviatoric-strain/pressure ($\mathbf{u}/\mathbf{e}/p$) FEs [25,28,29,34,67–70].

In this work, equal order linear interpolation functions are used for all unknown fields. A Variational Multiscale Stabilization procedure is adopted to circumvent the strictness of the Inf–Sup condition. The stabilization procedure modifies the discrete variational form within the framework of the VMS methods [5,62,63,65].

The idea of the VMS approach is to enhance the FE approximation of the continuous solution by adding to the discrete fields $\mathbf{u}_h$, $\mathbf{e}_h$, and p_h (from the FE space) a term $\tilde{\mathbf{u}}$, $\tilde{\mathbf{e}}$, and $\tilde{p}$ approximating the finer sub-grid scale that cannot be captured at the FE scale:

$$\begin{aligned} \mathbf{u} &\doteq \hat{\mathbf{u}} = \mathbf{u}_h + \tilde{\mathbf{u}} \\ \mathbf{e} &\doteq \hat{\mathbf{e}} = \mathbf{e}_h + \tilde{\mathbf{e}} \\ p &\doteq \hat{p} = p_h + \tilde{p} \end{aligned} \tag{42}$$

The Appendix details the derivation of the discrete stabilized formulation for the $\mathbf{u}/\mathbf{e}/p$ FEs.

The resulting stabilized FE system of equations is shown as Eq. (43) in Box I where $[\mathbf{U}\,\mathbf{E}\,\mathbf{P}]^T$ is the array of nodal values of displacements, deviatoric-strains and pressure and

$$\mathbf{K}^{\mathbf{e}}_{UU} = \int_\Omega \mathbf{B}_u^T\mathbf{C}^{dev}\mathbf{B}_u d\Omega \tag{44}$$

$$\mathbf{K}^{p}_{UU} = \int_\Omega \mathbf{N}_u^T\mathbf{G}\mathbf{G}^T\mathbf{N}_u d\Omega \tag{45}$$

$$\mathbf{K}_{EE} = \int_\Omega (\mathbf{N}_e^T\mathbf{S}\mathbf{C}^{dev})(\mathbf{C}^{dev}\mathbf{S}^T\mathbf{N}_e)d\Omega \tag{46}$$

$$\mathbf{K}_{PP} = \int_\Omega \mathbf{N}_p^T\mathbf{G}^T\mathbf{G}\mathbf{N}_p d\Omega \tag{47}$$

$$\begin{bmatrix} \tau_e\mathbf{K}^{\mathbf{e}}_{UU}+\tau_p\mathbf{K}^{p}_{UU} & (1-\tau_e)\mathbf{K}_{UE} & (1-\frac{\tau_p}{C^{vol}})\mathbf{K}_{UP} \\ (1-\tau_e)(\mathbf{K}_{UE})^T & -(1-\tau_e)\mathbf{M}_{EE}-\tau_u\mathbf{K}_{EE} & -\tau_u\mathbf{K}_{EP} \\ (1-\frac{\tau_p}{C^{vol}})(\mathbf{K}_{UP})^T & -\tau_u(\mathbf{K}_{EP})^T & -(1-\frac{\tau_p}{C^{vol}})\mathbf{M}_{PP}-\tau_u\mathbf{K}_{PP} \end{bmatrix} \begin{bmatrix} \mathbf{U} \\ \mathbf{E} \\ \mathbf{P} \end{bmatrix} = \begin{bmatrix} \mathbf{F} \\ \mathbf{0} \\ \mathbf{0} \end{bmatrix} \tag{43}$$

Box I.

$$\mathbf{K}_{EP} = \int_\Omega (\mathbf{N}_e^T \mathbf{S}\mathbf{C}^{dev})(\mathbf{G}\mathbf{N}_p)d\Omega \tag{48}$$

Note that the problem is symmetric and that for a converged solution (when $h \to 0$), the stabilization terms vanish. For non-converged situations these terms depend on the residual value of the system of equations. Varying the stabilization parameters τ_u, τ_e and τ_p produces slightly different results for a given FE mesh; however, the residual-based nature ensures the uniqueness of the solution upon mesh convergence. In linear problems, the optimal convergence rate is achieved using the stabilization parameters defined in Eq. (A.4) of the Appendix, which decrease on mesh refinement [71].

Finally, some remarks regarding the implementation of the formulation in FE codes are given.

Note that the $\mathbf{K}_{EE}$ and $\mathbf{K}_{EP}$ sub-matrices in Eqs. (46) and (48) can be rewritten as

$$\mathbf{K}_{EE} = \int_\Omega (\mathbf{B}_e\mathbf{C}^{dev})(\mathbf{C}^{dev}\mathbf{B}_e^T)d\Omega \tag{49}$$

$$\mathbf{K}_{EP} = \int_\Omega (\mathbf{B}_e\mathbf{C}^{dev})(\mathbf{G}\mathbf{N}_p)d\Omega \tag{50}$$

where $\mathbf{B}_e^{(i)}$ is a submatrix with an analogous structure to $\mathbf{B}_u^{(i)}$, defined for each node (i) of a given element as

$$\mathbf{B}_e^{(i)} = \mathbf{N}_e^{(i)T}\mathbf{S} = \begin{bmatrix} \partial_x N_e^{(i)} & 0 & 0 & \partial_y N_e^{(i)} & 0 & \partial_z N_e^{(i)} \\ 0 & \partial_y N_e^{(i)} & 0 & \partial_x N_e^{(i)} & \partial_z N_e^{(i)} & 0 \\ 0 & 0 & \partial_z N_e^{(i)} & 0 & \partial_y N_e^{(i)} & \partial_x N_e^{(i)} \end{bmatrix}^T \tag{51}$$

In this work, where the same interpolation functions are used for both the displacement and the deviatoric-strain, $\mathbf{B}_e$ and $\mathbf{B}_u$ are the same.

Note also that when using the same interpolation functions for both the displacement and the pressure, the submatrix $\mathbf{N}_u^T\mathbf{G}$ is equal to the submatrix $\mathbf{G}\mathbf{N}_p$. Specifically, it can be observed that, for each node (i) of a given element:

$$\mathbf{N}_u^{(i)T}\mathbf{G} = (\partial_x N_u^{(i)} \partial_y N_u^{(i)} \partial_z N_u^{(i)})^T \tag{52}$$

$$\mathbf{G}\mathbf{N}_p^{(i)} = (\partial_x N_p^{(i)} \partial_y N_p^{(i)} \partial_z N_p^{(i)})^T \tag{53}$$

3. Thermal problem and thermo-mechanical coupling

3.1. Strong form

The strong form of the thermal problem is written in terms of the temperature T as the energy balance equation

$$\rho c\dot{T} = -\nabla\cdot\mathbf{q} + \dot{R} + \dot{\mathcal{D}}_{mech} \text{ on } \Omega \tag{54}$$

where $\dot{T}$ is the temperature time derivative, $\rho = \rho(T)$ is the temperature-dependent material density, $c = c(T)$ is the temperature-dependent specific heat capacity of the material, $\dot{R}$ represents the heat source that may be present in the problem and $\dot{\mathcal{D}}_{mech}$ is the rate of mechanical dissipation that takes place in the body, dependent on the constitutive model employed. Here, the heat flux, $\mathbf{q}$, is computed according to the Fourier law

$$\mathbf{q} = -k\nabla T \tag{55}$$

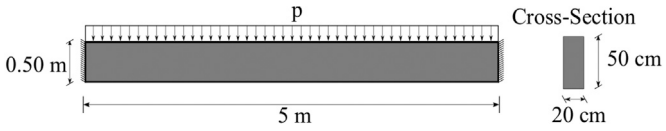

Fig. 1. Double clamped rectangular beam: Problem setting.

with $k = k(T)$ being the thermal conductivity of the material, also temperature-dependent. The left-hand side of Eq. (54) is the enthalpy rate where the heat capacity is $C = C(T) = \rho(T)c(T)$.

Introducing Eq. (55) in (54), the strong form becomes

$$C\dot{T} - \nabla\cdot(k\nabla T) = \dot{R} + \dot{\mathcal{D}}_{mech} \quad on\ \Omega \tag{56}$$

together with the prescribed thermal boundary conditions.

3.2. Weak form

Introducing δT as a virtual temperature field and integrating Eq. (56) over the domain Ω, the weak form of the energy balance is written as

$$\int_\Omega (\delta T C\dot{T})d\Omega + \int_\Omega (k\nabla\delta T\cdot\nabla T)d\Omega = \int_\Omega [\delta T(\dot{R}+\dot{\mathcal{D}}_{mech})]d\Omega + \int_{\Gamma_q}(\delta T\bar{q})d\Gamma \tag{57}$$

where the divergence theorem has been applied to the second term. The domain is closed by a smooth boundary Γ, such that $\Gamma = \Gamma_T \cup \Gamma_q$ and $\Gamma_T \cap \Gamma_q = \varnothing$, where Γ_T and Γ_q are the boundaries with prescribed temperatures and fluxes respectively. It is assumed that the prescribed temperatures vanish at the boundary Γ_T. The prescribed heat fluxes in the boundary Γ_q are noted $\bar{q}$.

The initial conditions are defined in terms of the initial temperature field at $t = 0$, where $T(t=0) = T_0$.

3.3. FE approximation

Similarly to the mechanical problem, the domain Ω is discretized in a FE partition such that $\Omega = \cup\Omega_e$, with the temperature and virtual temperature fields approximated according to the Galerkin method

$$\begin{aligned} T &\doteq \hat{T} = \mathbf{N}_T\mathbf{T} \\ \delta T &\doteq \delta\hat{T} = \mathbf{N}_T\delta\mathbf{T} \end{aligned} \tag{58}$$

where $\mathbf{T}$ and $\delta\mathbf{T}$ are the finite element nodal temperature and virtual temperature vectors, respectively, and $\mathbf{N}_T$ is the matrix containing the interpolation function adopted.

Introducing the FE discrete approximations into the continuous weak form of Eq. (57), results in

$$\begin{aligned} &\int_\Omega \delta\mathbf{T}^T\mathbf{N}_T^T C\mathbf{N}_T\dot{\mathbf{T}}d\Omega + \int_\Omega \delta\mathbf{T}^T\mathbf{N}_T^T\mathbf{G}^T k\mathbf{G}\mathbf{N}_T\mathbf{T}d\Omega \\ &= \int_\Omega \delta\mathbf{T}^T\mathbf{N}_T^T(\dot{R}+\dot{\mathcal{D}}_{mech})d\Omega + \int_{\Gamma_q}(\delta\mathbf{T}^T\mathbf{N}_T^T\bar{q})d\Gamma \ \forall\delta\mathbf{T} \end{aligned} \tag{59}$$

and the choice of the virtual field is arbitrary, thus the Galerkin approximation of Eq. (59) is

$$\int_\Omega \mathbf{N}_T^T C\mathbf{N}_T d\Omega\dot{\mathbf{T}} + \int_\Omega \mathbf{B}_T^T k\mathbf{B}_T d\Omega\mathbf{T} = \int_\Omega \mathbf{N}_T^T(\dot{R}+\dot{\mathcal{D}}_{mech})d\Omega + \int_{\Gamma_q}(\mathbf{N}_T^T\bar{q})d\Gamma$$

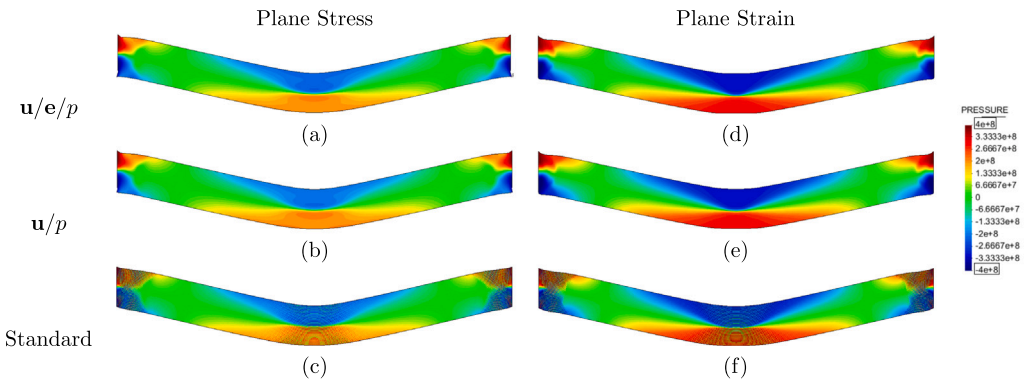

Fig. 2. Double clamped rectangular beam: Pressure in [Pa]. Plane-stress (*a*)–(*c*). Plane-strain (*d*)–(*f*).

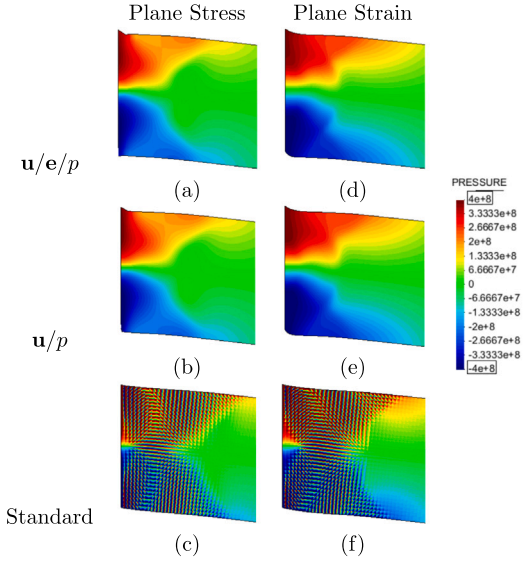

Fig. 3. Double clamped rectangular beam: Pressure in [Pa] at the left support. Plane-stress (*a*)–(*c*). Plane-strain (*d*)–(*f*).

(60)

with $\mathbf{B}_T = \mathbf{G}\mathbf{N}_T$.

3.4. Thermo-mechanical coupling

The coupled thermo-mechanical problem considered in this work is established in strong form by Eqs. (23) and (56). The corresponding discrete weak form of the problem being numerically computed is determined by Eqs. (43) and (60).

The time integration scheme adopted in Refs. [72–75] is considered to solve the discrete problem in time. The two sub-problems, mechanical and thermal, are solved sequentially following a staggered incremental procedure. When the mechanical dissipation is much lower than the energy input from the heat source, the thermo-mechanical coupling is weak, and a staggered solution of the thermal and the mechanical sub-problems is preferred instead of a monolithic approach.

For every time increment $\Delta t = t_{n+1} - t_n$ between time steps t_n and t_{n+1}, to obtain the solution at time t_{n+1}, first the mechanical sub-problem is calculated with all the state variables of the solution known at time instant t_n. This results in an intermediate solution, which is then used as a starting point to compute the thermal problem. According to the considerations in Ref. [74], the proposed algorithm does not need an iterative loop over the two sub-problems within the same time-step to ensure the convergence of the solution.

Due to the nonlinearity of the mechanical sub-problem, which includes J2-damage and J2-plasticity constitutive laws, an iterative Picard algorithm is introduced for its solution. Also, temperature-dependent mechanical properties are introduced, which are determined at t_{n+1} using the temperature computed at t_n.

As the thermal sub-problem in Eq. (60) involves the time derivatives of the temperature, an implicit Euler scheme is adopted for its solution. Temperature-dependent thermal properties are introduced as well, making the problem nonlinear. However, the resulting thermal sub-problem is solved in an incrementally linear manner. For this, material properties are also computed at time step t_{n+1} using the temperature field obtained at t_n.

For additional details on the thermo-mechanical coupling, Refs. [72–75] are recommended.

4. Constitutive laws

The mixed $\mathbf{u}/\mathbf{e}/p$ formulation requires the split of the constitutive law into the volumetric and deviatoric parts as shown in Eqs. (8) and (9). This section introduces the J2-damage and J2-plasticity laws used in this work to model the nonlinear material behavior in structural failure problems. The damage and yield surfaces of both models are described by the *Von Mises* criterion. Both models are comprehensibly described in Ref. [35]. For additional details on the constitutive laws, Ref. [35] is recommended.

4.1. J2-damage

In this section, the J2-damage model is presented. An isotropic damage model is considered for the deviatoric secant constitutive matrix $\mathbf{C}^{dev}$

$$\mathbf{C}^{dev} = (1 - d_s)\mathbf{C}_0^{dev} \tag{61}$$

where $\mathbf{C}_0^{dev}$ is the initial elastic deviatoric constitutive matrix and d_s is a damage variable modeling the degradation of the material, which ranges $0 \leqslant d_s \leqslant 1$.

The effective deviatoric-stress $\bar{\mathbf{s}}$ is defined as $\bar{\mathbf{s}} = \mathbf{C}_0^{dev}\mathbf{e}$ and the corresponding equivalent effective deviatoric-stress τ is

$$\tau = \sqrt{\frac{3}{2}}\,\|\bar{\mathbf{s}}\| = \sqrt{\frac{3}{2}}\left[\bar{\mathbf{s}}^T\bar{\mathbf{s}}\right]^{1/2} \tag{62}$$

The damage criterion, $\mathcal{F}_d$, is

$$\mathcal{F}_d = \tau - r(\bar{\mathbf{s}}) \leqslant 0 \tag{63}$$

where r is the current damage threshold. Its initial value is the tensile strength of the material, $r_0 = \sigma_y$. According to the Kuhn–Tucker optimality and consistency conditions, the value of the damage threshold at time t is explicitly updated as

$$r(\bar{\mathbf{s}}) = \max(r_0, \max \tau(\hat{t})) \qquad \hat{t} \in [0, t] \tag{64}$$

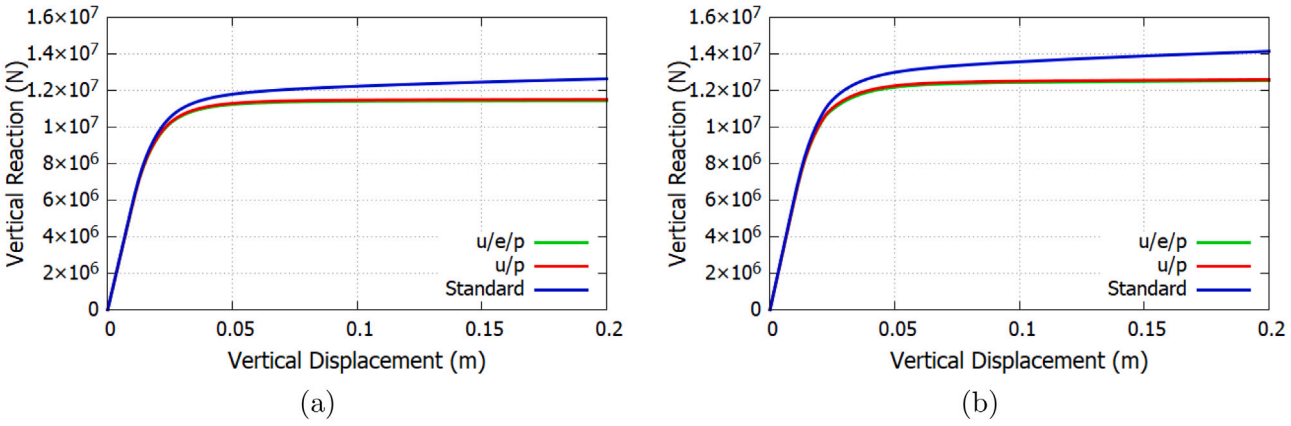

Fig. 4. Double clamped rectangular beam: Vertical reaction (*half*) vs vertical displacement. (*a*) Plane-stress. (*b*) Plane-strain.

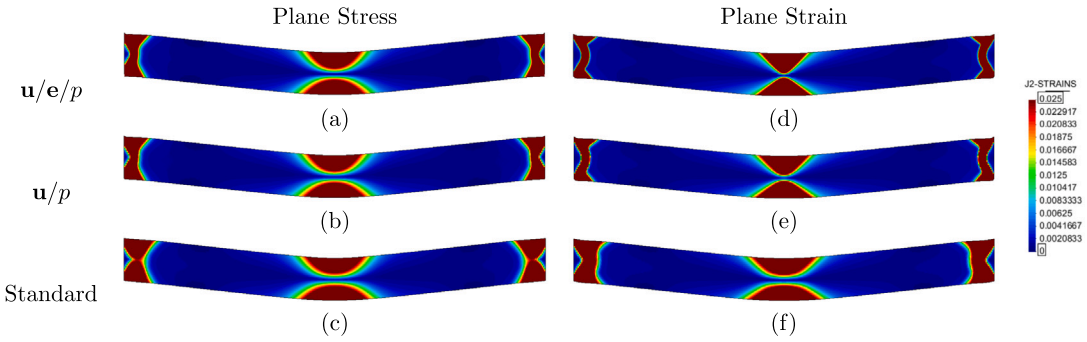

Fig. 5. Double clamped rectangular beam: J2-strains. Plane-stress (*a*)–(*c*). Plane-strain (*d*)–(*f*).

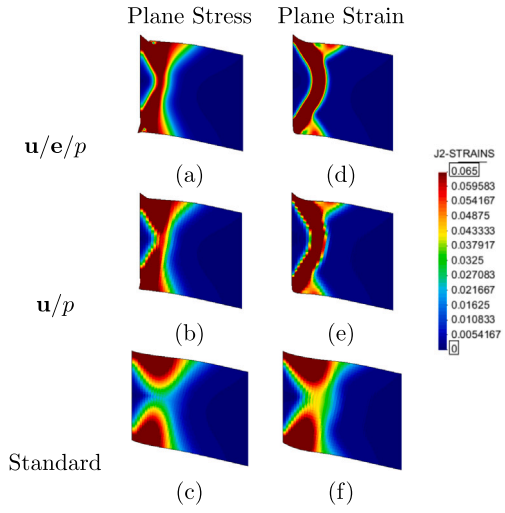

Fig. 6. Double clamped rectangular beam: J2-strains detail at the left support. Plane-stress (*a*)–(*c*). Plane-strain (*d*)–(*f*).

The evolution of the internal damage variable is defined by

$$d_s = d_s(r) = 1 - \frac{r_0}{r}\exp\left(-2H_S\left(\frac{\langle r - r_0\rangle}{r_0}\right)\right) \tag{65}$$

where H_S is a positive softening parameter controlling the rate of material degradation and $\langle\cdot\rangle$ are the Macaulay brackets such that $\langle x\rangle = x$ if $x \geqslant 0$, $\langle x\rangle = 0$ if $x < 0$.

The mechanical dissipation $\dot{\mathcal{D}}_{mech}$ for this constitutive law is

$$\dot{\mathcal{D}}_{mech} = \psi_0 \dot{d}_s = \frac{1}{2}\mathbf{e}^T \mathbf{C}_0^{dev}\mathbf{e}\dot{d}_s \geq \mathbf{0} \tag{66}$$

where $\psi_0 = \frac{1}{2}\mathbf{e}^T \mathbf{C}_0^{dev}\mathbf{e}$ is the initial elastic strain energy density per unit of volume of the undamaged material and $\dot{d}_s$ is the derivative of the damage d_s with respect to time.

The total dissipation along the process is [35]

$$\mathcal{D}_{mech} = \int_{t=0}^{t=\infty} \dot{\mathcal{D}}_{mech}dt = \int_0^{\infty} \frac{1}{2}\mathbf{e}^T \mathbf{C}_0^{dev}\mathbf{e}\dot{d}_s dt = W_0^e + \frac{W_0^e}{H_S} \tag{67}$$

where W_0^e is the maximum energy per unit volume that can be absorbed up to the elastic limit without permanent damage. For the case of isotropic materials, $W_0^e = \frac{1}{2}\frac{(\sigma_y)^2}{3G_0}$, G_0 being the initial elastic shear modulus. The previous expression of $\mathcal{D}_{mech}$ can be related to the fracture energy $\mathcal{G}_f$ as [76,77]

$$\mathcal{D}_{mech} = \frac{\mathcal{G}_f}{b} \tag{68}$$

where b is the bandwidth of the strain localization, which is equal to $2h$ for the 3-field element, h being the FE size. This results in

$$H_S = \frac{\bar{H}_S b}{1 - \bar{H}_S b} \tag{69}$$

$$\bar{H}_S = \frac{(\sigma_y)^2}{6G_0\mathcal{G}_f} \tag{70}$$

Eqs. (64)–(66) guarantee the irreversible nature and the positiveness of the dissipation.

4.2. J2-plasticity

Herein, the J2-plasticity model is presented. The deviatoric plastic strains $\mathbf{e}^p$ are introduced as

$$\mathbf{s} = \mathbf{C}_0^{dev}\mathbf{e}^e = \mathbf{C}_0^{dev}(\mathbf{e} - \mathbf{e}^p) \tag{71}$$

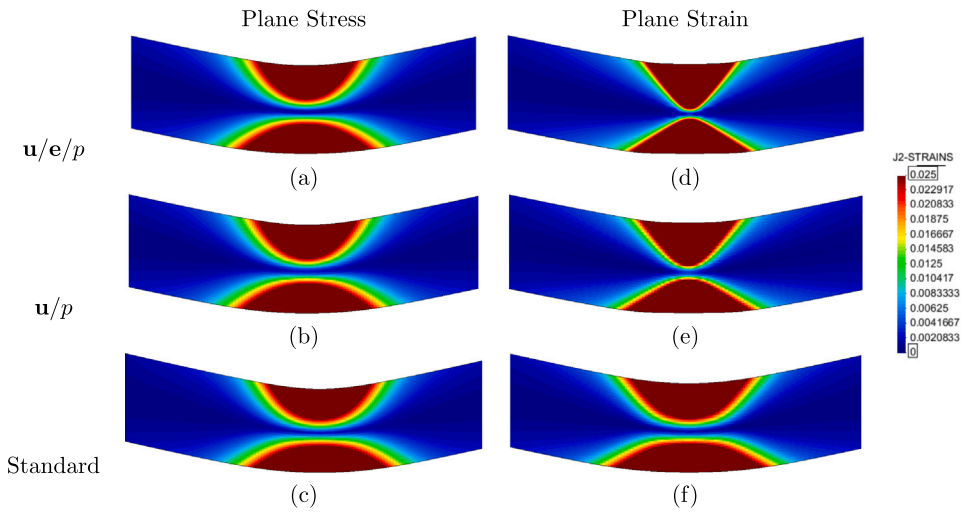

Fig. 7. Double clamped rectangular beam: J2-strains detail at the center of the beam. Plane-stress (*a*)–(*c*). Plane-strain (*d*)–(*f*).

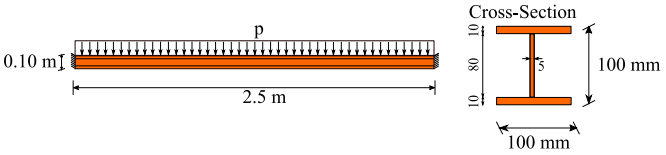

Fig. 8. Double clamped I-shaped beam: Problem setting.

where $\mathbf{C}_0^{dev}$ is the deviatoric part of the elastic constitutive matrix and $\mathbf{e}^e$ are the deviatoric elastic strains computed as

$$\mathbf{e}^e = \mathbf{e} - \mathbf{e}^p \tag{72}$$

The constitutive equation can be rewritten in terms of the secant deviatoric constitutive matrix

$$\mathbf{s} = \left[\mathbf{C}_0^{dev} - \frac{(\mathbf{C}_0^{dev}\mathbf{e}^p)(\mathbf{C}_0^{dev}\mathbf{e}^p)^T}{\mathbf{e}^T\mathbf{C}_0^{dev}\mathbf{e}^p}\right]\mathbf{e} = \mathbf{C}^{dev}\mathbf{e} \tag{73}$$

where $\mathbf{C}^{dev}$ is the deviatoric part of the secant nonlinear constitutive tensor, which is symmetric by construction.

Taking into account that, for an isotropic material, $\mathbf{C}_0^{dev} = 2G_0\mathbf{Y}$, that $\mathbf{e} = \mathbf{Ye}$ and that $\mathbf{e}^p$ is also purely deviatoric i.e. $\mathbf{e}^p = \mathbf{Ye}^p$, Eq. (73) can be simplified to

$$\mathbf{s} = 2G_0\left[\mathbf{J} - \frac{\mathbf{e}^p(\mathbf{e}^p)^T}{\mathbf{e}^T\mathbf{e}^p}\right]\mathbf{e} \tag{74}$$

Using the equivalent deviatoric-stress, τ, defined in Eq. (62), the plastic yield surface, $\mathcal{F}_p$, is defined as

$$\mathcal{F}_p = \tau - r_p(q) \leqslant 0 \tag{75}$$

where $r_p(q)$ are the admissible deviatoric-stresses, and q is a stress-like internal variable that controls the *softening* of the model. The deviatoric stress threshold is

$$r_p(q) = \sigma_y - q(\xi) \tag{76}$$

where σ_y is the initial uniaxial stress threshold, ξ is the equivalent plastic strain and $q(\xi)$ is the softening function, that in this work is exponential:

$$\xi = \sqrt{\frac{2}{3}}\,\|\mathbf{e}^p\| \tag{77}$$

$$q(\xi) = \sigma_y \exp\left(\frac{-2H}{\sigma_y}\xi\right) \qquad \text{for } 0 \leqslant \xi \leqslant \infty \tag{78}$$

where H is the softening parameter.

The plastic evolution laws are

$$\dot{\mathbf{e}}^p = \dot{\lambda}\mathbf{n} \tag{79}$$

$$\dot{\xi} = \dot{\lambda}\sqrt{\frac{2}{3}} \tag{80}$$

where $\dot{\lambda}$ is the plastic multiplier determined by the Kuhn–Tucker optimality and consistency conditions and $\mathbf{n}$ is the normal to the yield surface, defined by

$$\mathbf{n} = \frac{\partial \mathcal{F}_p}{\partial \mathbf{s}} = \frac{\mathbf{s}}{\|\mathbf{s}\|} \tag{81}$$

The rate of plastic work is $\dot{\mathcal{D}}_{mech} = \mathbf{s} : \dot{\mathbf{e}}^p$ and the total deviatoric plastic work along the softening process is

$$\mathcal{D}_{mech} = \int_{t=0}^{t=\infty} \dot{\mathcal{D}}_{mech}\,dt = \int_0^\infty q(\xi)d\xi = \frac{\sigma_y^2}{2H} \tag{82}$$

Also, the dissipated energy in a softening process can be related to the fracture energy $\mathcal{G}_f$ as

$$\mathcal{D}_{mech} = \frac{\mathcal{G}_f}{b} = \frac{\mathcal{G}_f}{2h} \tag{83}$$

where b is the bandwidth of the strain localization, that in this work is $2h$ for the 3-field element, h being the mesh size.

Finally, the softening parameter H can be computed using Eq. (82) and (83) as

$$H = \frac{\sigma_y^2}{2\mathcal{G}_f}b = 2h\bar{H} \tag{84}$$

$$\bar{H} = \frac{\sigma_y^2}{2\mathcal{G}_f} \tag{85}$$

The parameter H depends on the mesh resolution h and the material properties.

5. Numerical simulations

In this section, the enhanced accuracy and the mesh independence of the mixed $\mathbf{u}/\mathbf{e}/p$ formulation are assessed in isothermal (Section 5.1) and non-isothermal (Sections 5.2–5.5) failure problems. Temperature-dependent properties are considered. The simulations include the J2-damage and J2-plasticity constitutive models, introducing the isochoric behavior into the problem; thus the requirement of using a FE approach such as $\mathbf{u}/\mathbf{e}/p$, capable of resolving incompressible conditions. Several FE discretizations (triangular, quadrilaterals and hexahedral elements) are used to show the generality of the formulation.

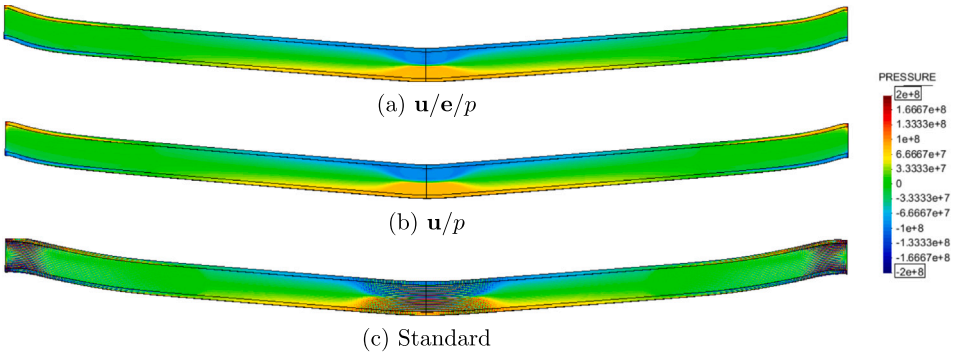

Fig. 9. Double clamped I-shaped beam: Pressure in [Pa].

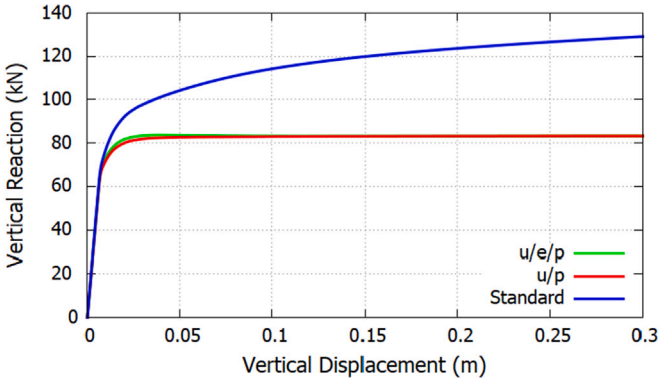

Fig. 10. Double clamped I-shaped beam: Vertical reaction (*half*) vs vertical displacement.

The nonlinear problem is solved incrementally in a (pseudo) time step-by-step manner; at each step a staggered scheme is used for the mechanical and the thermal problems. An iterative Picard algorithm is employed in the mechanical problem. A convergence based on the norm of the residuals of Eqs. (43) with a tolerance of 10^{-5} is adopted at each time step. The thermal problem is solved in a linear incremental manner and an implicit backward Euler scheme is adopted for its resolution.

The mixed $\mathbf{u}/\mathbf{e}/p$ formulation is compared with the $\mathbf{u}/p$ FE in terms of result accuracy, collapse mechanism prediction and numerical stability. The approximations adopted are *Q1Q1* and *P1P1* for $\mathbf{u}/p$ and *Q1Q1Q1* and *P1P1P1* for $\mathbf{u}/\mathbf{e}/p$ in the mechanical simulation and *Q1* and *P1* for the thermal field, depending on the FE discretization.

The stabilization constants defined in Eq. (A.4) of the Appendix are taken as $L_0 = 1.0$, $c_u = 1.0$, $c_p = 0.0$ and $c_e = 0.1$ for both the $\mathbf{u}/p$ and $\mathbf{u}/\mathbf{e}/p$ formulations.

An enhanced version of the finite element code COMET (see [78]), developed by the authors, is used to solve the numerical simulations. The pre and post process is done with GiD, a software developed at the International Center for Numerical Methods in Engineering (CIMNE) [79]. Paraview [80] is used for post processing as well.

5.1. Double clamped beam

5.1.1. Rectangular beam

In this section the development of plastic hinges is studied in a clamped–clamped beam in plane-stress and plane-strain conditions. In the present examination, the performance of the standard, $\mathbf{u}/p$ and $\mathbf{u}/\mathbf{e}/p$ FE formulations are investigated when used in conjunction with an isochoric (incompressible) nonlinear constitutive model. The numerical simulations compare their solution in an isothermal setting. The geometry and loading conditions of the beam are shown in Fig. 1.

The collapse mechanism predicted from the limit analysis of the beam consists in the formation of two plastic hinges at the clamped ends and, ultimately, of a third plastic hinge at the center of the beam.

The constitutive model adopted is elasto-perfect J2-Plasticity with a Young's modulus of $E = 200\,[\text{GPa}]$, Poisson's ratio of $\nu = 0.3$ and an uniaxial yield stress threshold of $\sigma_y = 500\,[\text{MPa}]$. For the plane-stress assumption, where the transversal stress is $\sigma_z = 0$, the theoretical ultimate distributed load is $p_u = 4000$ [kN/m] and the vertical reaction in each end is 10,000 [kN]. For the plane-strain case, the influence of $\sigma_z \neq 0$ reflects on the perceived yield threshold, $\bar{\sigma}_y \geq \sigma_y$ [81], which, in the case of the Von Mises criterion, is given by

$$\bar{\sigma}_y = \frac{\sigma_y}{\sqrt{1 - \nu + \nu^2}}$$

so, the corresponding plane-strain condition ultimate load is $p_u = 4500$ [kN/m] resulting in a vertical reaction of 11,250 [kN] in each end.

A structured quadrilateral mesh is adopted and, due to the symmetry of the problem, half of the domain is considered, with a total of 5494 elements and a FE size of $h = 0.015$ [m]. An arc-length strategy is used in the simulations, controlling the displacement at the top midpoint.

Fig. 2 shows the pressure computed in plane-stress and plane-strain conditions for the standard, $\mathbf{u}/p$ and $\mathbf{u}/\mathbf{e}/p$ FEs. The standard element presents spurious oscillations of the pressure field while the mixed formulations provide a smooth (correct) solution. Fig. 3 shows the detail of the pressure at the left support where the poor performance of the standard element is noticeable.

Fig. 4 shows the vertical reaction of one clamped end *versus* the vertical displacement of the mid-span. In this simulation without material softening, the two mixed FE formulations coincide while the standard formulation presents a spurious hardening behavior due to the volumetric locking that takes place in the computed solution. This shows the inability of the standard FE formulation in reproducing nonlinear isochoric behavior such as J2-plasticity.

Fig. 5 shows the J2-strains for the three FEs formulations. It can be seen that the plastic hinges at the clamped ends form an arch that connects the top and bottom faces of the beam. Close to the clamped end, a region with no strain localization that extends towards the center of the beam can be observed. The support and central hinges are detailed in Figs. 6 and 7, respectively.

The numerical results in terms of load capacity in Fig. 4 for plane-stress are higher than the theoretical results derived from the plastic limit analysis. This is because of the assumption that the plastic hinge develops exactly at the clamped face of the beam, which limit analysis translates into assuming that the effective span coincides with the geometric span. Fig. 5 shows that this is not the case; a dead-region is formed, which decreases the value of the effective span length, considered to be the distance from hinge to hinge, and increases the ultimate load. In the plane stress case, the maximum vertical reaction in $\mathbf{u}/\mathbf{e}/p$ is 11,440 [kN], for the $\mathbf{u}/p$ is 11,510 [kN] and for the standard

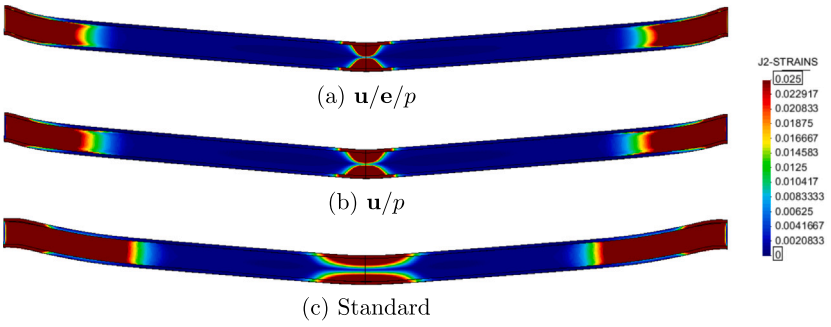

Fig. 11. Double clamped I-shaped beam: J2-strains.

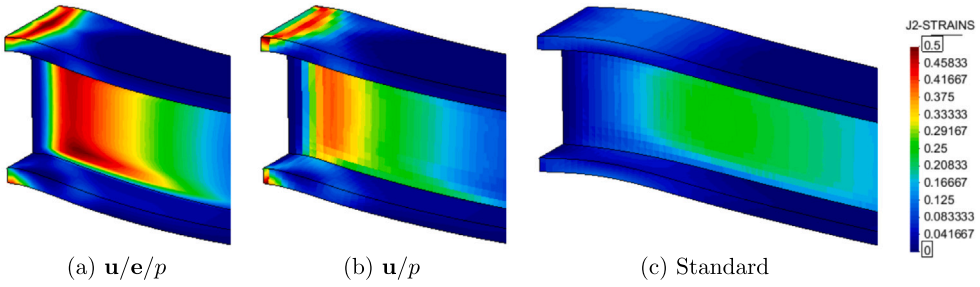

Fig. 12. Double clamped I-shaped beam: J2-strains detail at the left clamped-end.

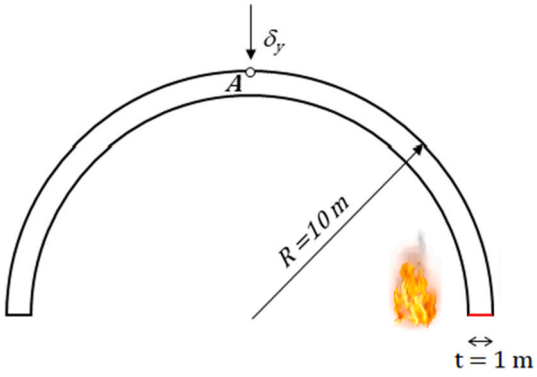

Fig. 13. Semicircular arch: Problem setting.

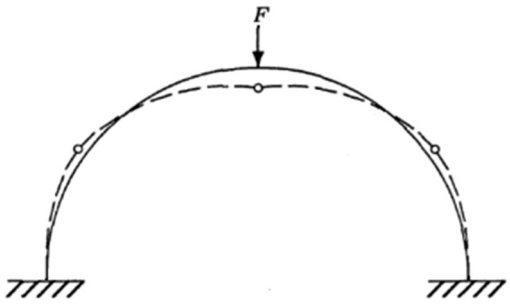

Fig. 14. Semicircular arch: Collapse mechanism in an isothermal setting in dashed line. *Source:* Adapted from [81].

formulation is 12,640 [kN] at $\delta_y = 0.20$ [m]; the theoretical one when adopting a reduced effective span of $L_{eff} = 4.52$ [m], as observed in the numerical solution, is 11,060 [kN].

5.1.2. I-shaped beam

In the following, the numerical simulation of the formation of plastic hinges is considered in an I-shaped beam. The goal of this section is to analyze the phenomenon in a 3D geometry, where the cross section of the beam does not have constant width.

Fig. 8 shows the geometry and boundary conditions of this case. The analysis is performed using elasto-perfect J2-plasticity, with a Young modulus $E = 200$ [GPa], Poisson's ratio of $\nu = 0.3$ and an uniaxial yield stress threshold $\sigma_y = 245$ [MPa]. Considering the geometrical span length $L = 2.5$ [m], as shown in Fig. 8, the theoretical ultimate load of the beam is $p = 61.47$ [kN/m]. This results in a vertical reaction on each end of $R = 76.8$ [kN].

Due to symmetry, half of the problem is considered. The simulation is performed using an arc-length strategy controlling the vertical displacement at the beam top midpoint. The domain is discretized using a structured mesh of hexahedral elements of size $h = 5 \cdot 10^{-3}$ [m], with a total of 25,000 elements. At one end the beam is clamped and at the mid-span symmetry conditions are applied.

Fig. 9 shows the pressure for the three FEs, where it can be seen that the solution obtained by the standard formulation suffers from spurious oscillations. Fig. 10 shows the evolution of the vertical reaction at the left clamped end with the vertical displacement at the mid-span. In this simulation without material softening, both mixed formulations reach similar final bearing capacities, with the $\mathbf{u}/\mathbf{e}/p$ value being 83.1 [kN] and the $\mathbf{u}/p$ value 83.4 [kN], while the standard FE produces a much stiffer solution due to the volumetric locking originated by the incapability of the standard element to address the material isochoric (incompressible) behavior.

Fig. 11 presents the J2-strains for the three formulations where a slightly different strain distribution on the web is observed between

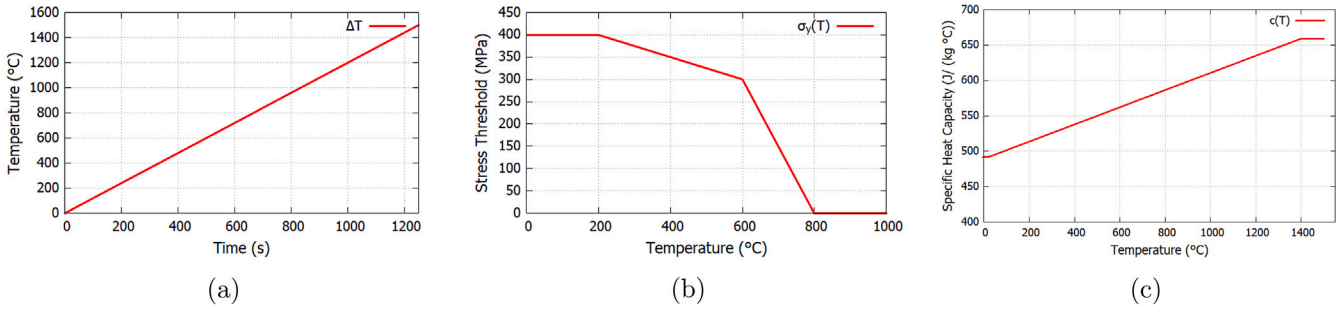

Fig. 15. Semicircular arch: (*a*) Heat source increment over time. Evolution of the (*b*) stress threshold and (*c*) specific heat capacity with temperature.

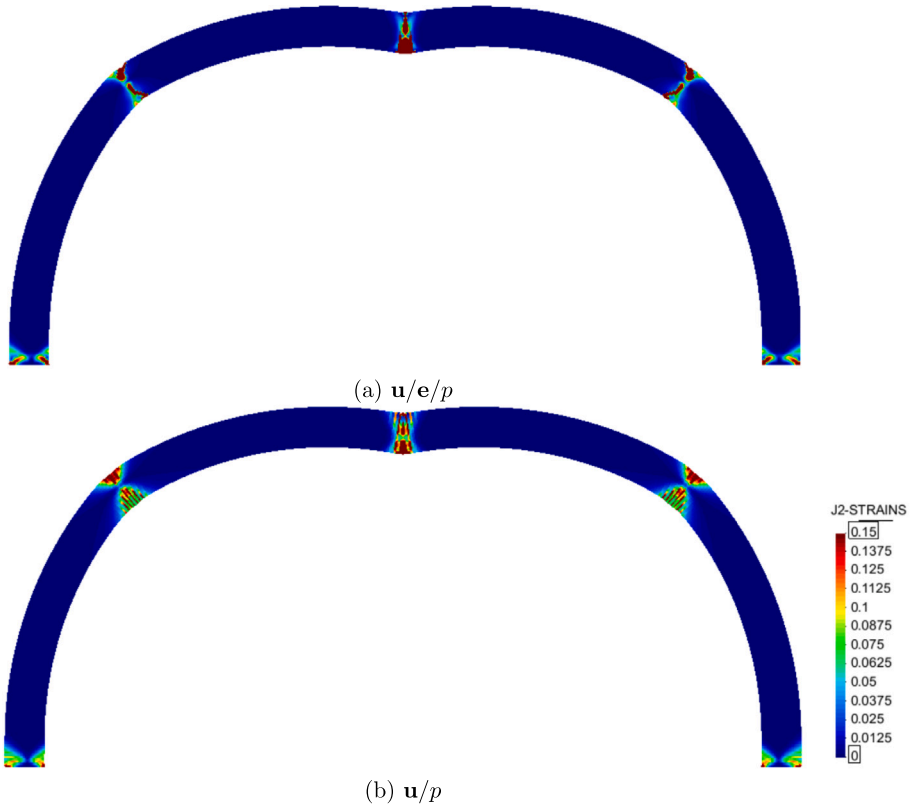

Fig. 16. Semicircular arch: Reference model (isothermal) failure mechanism for $\delta_y = 1.6\,[\mathrm{m}]$.

the mixed formulations. The J2-strains for the $\mathbf{u}/p$ element are more uniform throughout the web height. Fig. 12 provides a zoom at the clamped end for a total displacement of $|\delta| = 0.30\,[\mathrm{m}]$. The $\mathbf{u}/p$ formulation has a lower accuracy in terms of strains and is not able to capture the distribution observed in the 3-field solution. The standard formulation presents a much broader area where the J2-strains develop, Fig. 11, but the J2-strains magnitude are much smaller than the mixed formulations values, Fig. 12, due to the volumetric locking of the standard element.

It can be seen in Fig. 12 how also in this case a dead region where no localization occurs develops next to the clamped face of the beam. This reduces the effective span length of the beam to $L_{eff} = 2.45\,[\mathrm{m}]$. The resulting ultimate load is $p = 64\,[\mathrm{kN/m}]$, and the expected vertical reaction at each beam end (half vertical reaction) is $R = 80\,[\mathrm{kN}]$. The load capacities observed in Fig. 10 when using the $\mathbf{u}/p$ and $\mathbf{u}/\mathbf{e}/p$ FEs agree with these values.

5.2. Semicircular arch

In the next simulation, a semicircular arch in plane-stress conditions is considered with temperature-dependent material properties. A heat source is placed at one end of the arch, weakening the bearing capacity. The aim of this example is to assess the difference in the failure mechanisms provided by the 3-field and $\mathbf{u}/p$ solutions.

The arch is clamped in both ends and has an outer radius $R = 10\,[\mathrm{m}]$, a thickness $t = 1.0\,[\mathrm{m}]$, a width $\omega = 0.5\,[\mathrm{m}]$ and is subjected to a vertical displacement $\delta_y = 2.5\,[\mathrm{m}]$ downwards with a heat source placed on the right clamping (see Fig. 13). Fig. 13 shows the point A chosen to measure the evolution of the temperature.

An isothermal reference case is also considered to assess the influence of the temperature on the failure mechanism. The structure, if not subjected to temperature effects, fails with the formation of symmetrical hinges [81] as presented in Fig. 14.

The constitutive model adopted is the isotropic J2-Damage and the material properties are described in Table 2. The heat load is described

Table 2
Semicircular arch: Material properties.

Property	Value
Young's Modulus [GPa]	200
Fracture Energy [MJ/m^2]	60
Density [kg/m^3]	7800
Thermal Conductivity [W/(m °C)]	45
Thermal Expansion coefficient [m/(m °C)]	$12 \cdot 10^{-6}$

in Fig. 15(*a*). The yield stress threshold, σ_y, and the specific heat capacity, c, vary in function of the temperature, see Fig. 15(*b*) and (*c*). These evolution functions of the material temperature-dependency are taken based on the behavior reported for steel in Ref. [82].

A structured quadrilateral mesh with 16 elements through the thickness is adopted, resulting in a total of 8000 elements with an average size of $h = 0.0625$ [m].

Fig. 16 shows the failure mechanism for the isothermal case, comparable to the expected behavior in Fig. 14. Fig. 17 details the evolution of the intermediate plastic hinge in four different time steps. The lack of accuracy of the $\mathbf{u}/p$ formulation introduces stress locking, precludes the achievement of a localized solution and exhibits the banding phenomenon in Fig. 17*c* (*right*), in contrast to the $\mathbf{u}/\mathbf{e}/p$ result. This increases the mechanical dissipation 32.2% for the $\mathbf{u}/p$ element compared to the 3-field solution, as can also be seen in the reaction vs displacement plot in Fig. 18(*a*). This also produces an overestimation of the failure load by $\mathbf{u}/p$ of 2.29% with respect to the $\mathbf{u}/\mathbf{e}/p$, as can be appreciated in Fig. 18(*a*).

Fig. 19 shows the unsymmetrical failure mechanism induced by the heat source positioned at the right hand side base for the mixed $\mathbf{u}/\mathbf{e}/p$ and the mixed $\mathbf{u}/p$. The right base of the arch loses strength at a faster rate which produces the unsymmetrical failure mechanism. Although both solutions are unsymmetrical, a large difference is observed between both collapse mechanisms. The $\mathbf{u}/\mathbf{e}/p$ element yields a sliding mechanism, due to the loss of strength at the arch base, while the $\mathbf{u}/p$ displays a stiffer solution, resulting from the stress locking observed at the hinges.

Fig. 18 presents the vertical reaction vs displacement plot for the $\mathbf{u}/p$ and $\mathbf{u}/\mathbf{e}/p$ formulations (recall that the reference case is isothermal) and the temperature evolution at point A. The differences between the 3-field and the $\mathbf{u}/p$ solutions are caused by the formation of a different failure mechanism and the over dissipation exhibited by the $\mathbf{u}/p$, both originated from the poor evaluation of the stress/strain field. Note also that the resulting bearing capacities are different: $55,396\,kN$ for the $\mathbf{u}/p$ and $53,720\,kN$ for the $\mathbf{u}/\mathbf{e}/p$, a 3.12% difference. The heat increase at the base barely affects the peak load value with respect to the isothermal case, but the resulting nonlinear structural response is greatly modified. The measured temperature increase at point A, presented in Fig. 18(*b*), depends on the mechanical dissipation and captures the instant when the localization occurs, when the peak value is attained. The hinge is formed sooner in the $\mathbf{u}/\mathbf{e}/p$ solution, denoting that the $\mathbf{u}/p$ has a stiffer behavior and delays the localization process.

5.3. Temperature induced failure - 3D frame

The following example is a 3D frame subjected to self-weight. The structural failure is induced by an incremental heat source placed on the right portion of the beam–column connection, shown in Fig. 20 and defined in Fig. 21(*a*). The frame has a total height of 3 [m] with a free span of 4.8 [m]. The heat-affected area is a portion of the beam with 1.2 [m] in length from the right beam–column connection. The beam and column cross-sections are presented in Fig. 20.

The constitutive model is perfect J2-Plasticity, Young's modulus is $E = 200$ [GPa], the material density is $\rho = 7800$ [kg/m^3] and the thermal expansion coefficient is $\alpha = 12 \cdot 10^{-6}$ [m/(m °C)]. The yield stress threshold, σ_y, the specific heat capacity, c, and the thermal conductivity, k, are temperature dependent, as shown in Fig. 21 (*b*)–(*d*). The evolution laws are taken based on the behavior reported in Ref. [82]. The simulation is performed with a time step of 20 [s] in a total of 10,000 [s] and a structured hexahedral mesh with element size $h = 0.025$ [m] (39,936 elements in total).

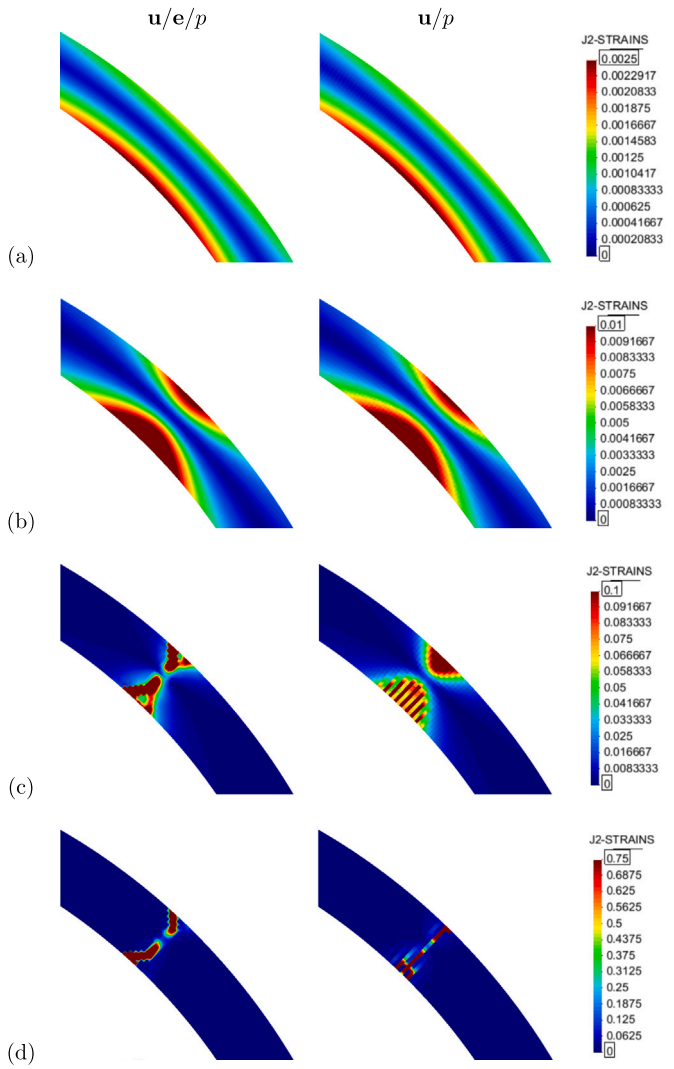

Fig. 17. Semicircular arch: Reference model (isothermal) detail of the development of the intermediate plastic hinge. (*a*) $\delta_y = 0.10$ [m]. (*b*) $\delta_y = 0.30$ [m]. (*c*) $\delta_y = 1.20$ [m]. (*d*) $\delta_y = 2.5$ [m].

Fig. 22 shows the evolution of the vertical reaction at each column. On the one hand, the $\mathbf{u}/p$ simulation stops at 3880 [s], when the temperature in the heated region reaches 796 °C, due to the degradation of the strength of the beam in the heated zone. On the other hand, the $\mathbf{u}/\mathbf{e}/p$ formulation manages to conclude the analysis successfully.

Figs. 23(*a*)–(*b*) shows the J2-strains developed by the mixed $\mathbf{u}/p$ and $\mathbf{u}/\mathbf{e}/p$ formulations a few time-steps before the mixed $\mathbf{u}/p$ formulation fails. This is caused by the lack of local convergence of the $\mathbf{u}/p$ formulation, which induces a premature shear mechanism at the heated beam–column connection, observed in the following time-step in Fig. 23(*c*)–(*d*). On the other hand, this does not happen in the enhanced accuracy mixed $\mathbf{u}/\mathbf{e}/p$ formulation and the analysis follows on until the final time-step $t = 10,000$ [s].

5.4. The Prandtl Punch test

The Prandtl Punch test consists of a rigid punch pressed into a semi-infinite domain in plane-strain conditions. The geometry considered is

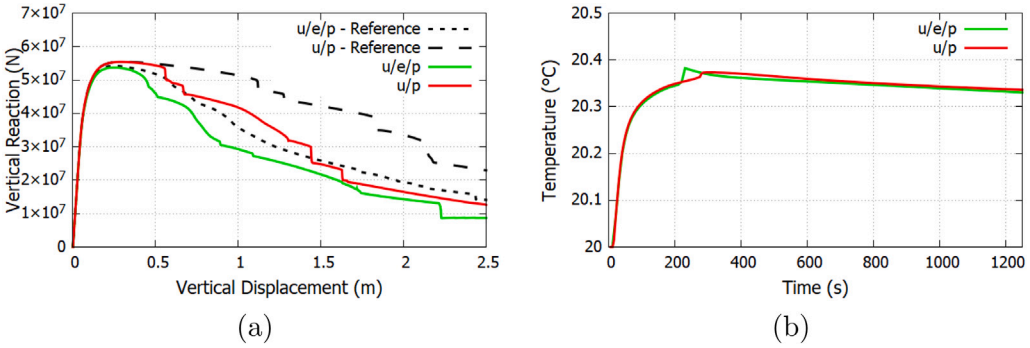

Fig. 18. Semicircular arch: (*a*) Reaction vs displacement curves and (*b*) temperature evolution over time at point *A*.

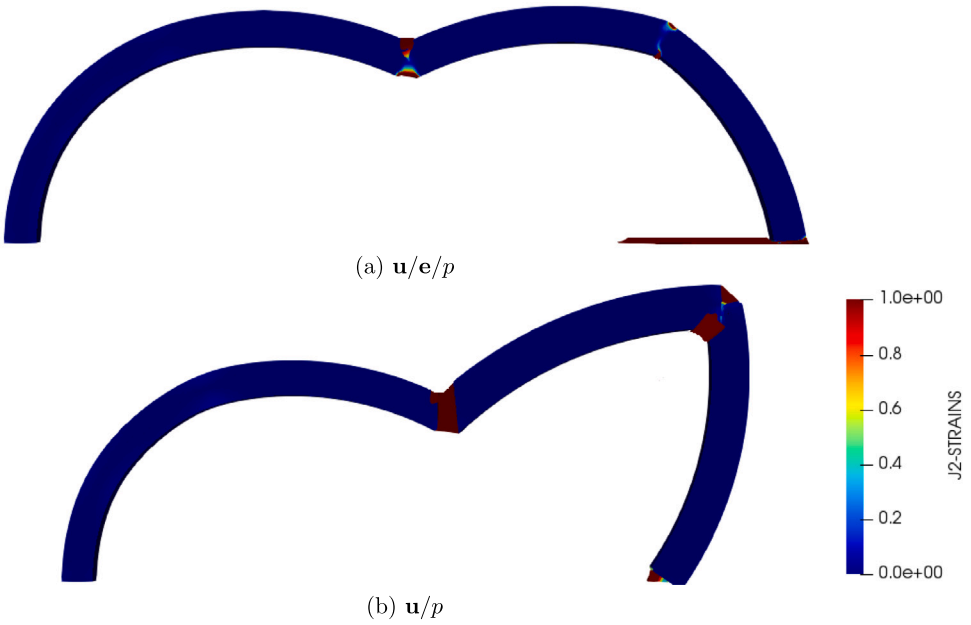

Fig. 19. Semicircular arch: Failure mechanism with heated base for $\delta_y = 2.50\,[\mathrm{m}]$.

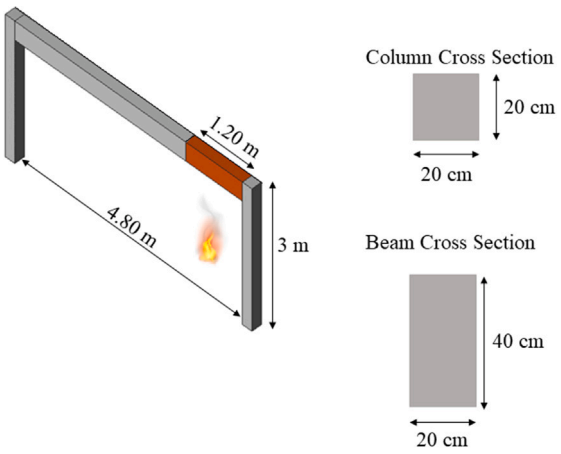

Fig. 20. 3D frame with heat source at the right quarter portion of the beam–column connection: Problem setting.

a 4 [m] × 2 [m] ($x \times y$) region with a rigid punch of size 1.0 [m] centered at the top portion of the domain (see Fig. 24). Due to the symmetry of the problem only half of the domain is considered.

Also, in this section, artificial properties are considered, to better demonstrate the capacities of both mixed FE formulations. The constitutive model is J2-Damage with a high value for the fracture energy ($G_f \longrightarrow \infty$). The material properties are Young's Modulus, $E = 10\,[\mathrm{MPa}]$, density, $\rho = 7800\,[\mathrm{kg/m^3}]$, Poisson's ratio $\nu = 0.5$ (incompressible elastic behavior), specific heat capacity, $c = 5{\cdot}10^{-5}\,[\mathrm{J/(kg\,°C)}]$, and the evolution of the yield-threshold with respect to the temperature is shown in Fig. 25. Two simulations, one with null thermal conductivity and one including an external heat source, are performed in this section. In this problem with elastic incompressible behavior, the pressure stabilization constant is set to $c_p = 0.1$.

Computations are conducted using a 14,608 unstructured triangular element mesh in the first case and a 6400 quadrilateral element discretization in the second one, with the element size being $h = 0.025$ [m] in both meshes. A downward vertical displacement of $\delta_y = 0.20$ [m] is applied to the rigid punch area in 500 [s] (500 steps).

The failure mechanism in an isothermal setting is shown in Fig. 26 with critical angles of $\theta = \pm 45°$ from the edge of the punch with the horizontal plane. The analytical peak load (yield load), q, for the rigid

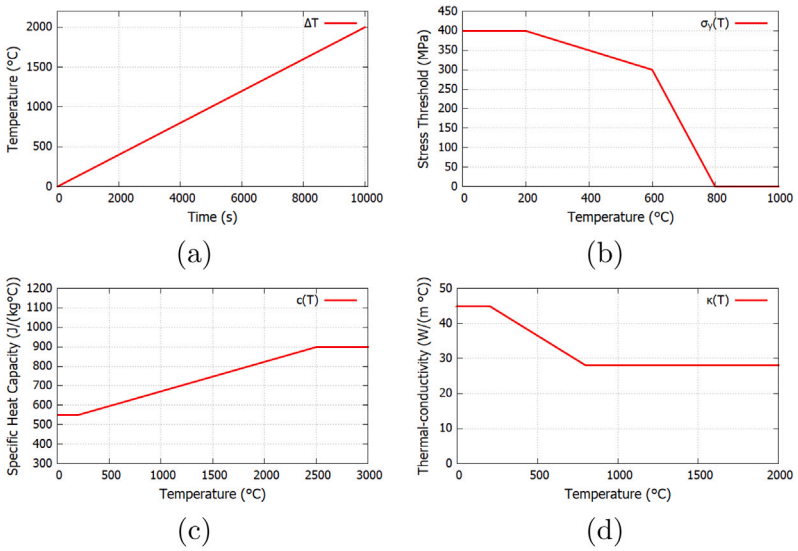

Fig. 21. 3D frame: (*a*) Heat source increment over time. (*b*) Uniaxial stress threshold, (*c*) Specific heat capacity, (*d*) Thermal conductivity, evolution with the temperature.

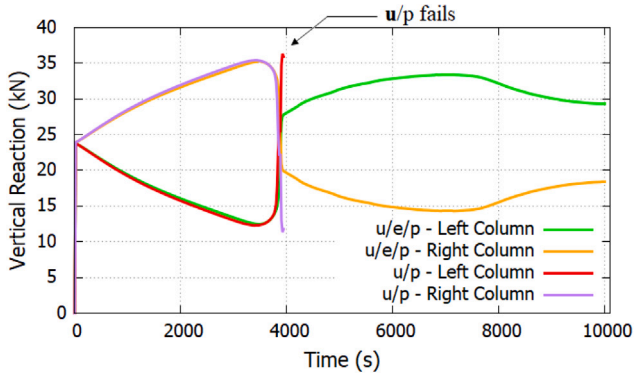

Fig. 22. 3D frame: Evolution curves of the bearing capacity of the columns.

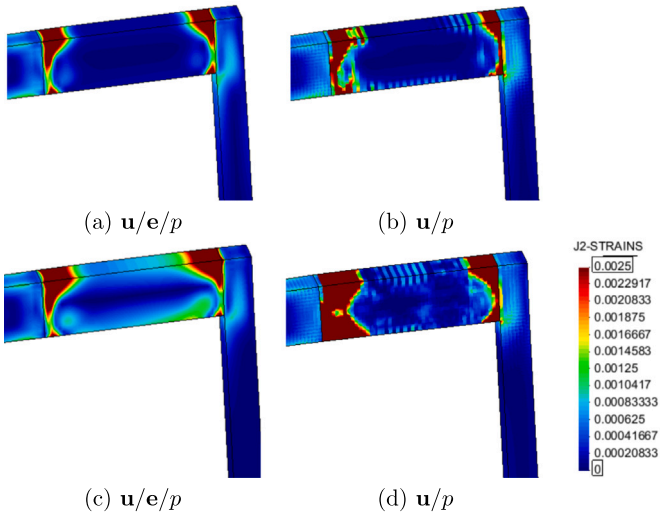

Fig. 23. 3D frame: J2-strains at the beam–column connection (*a*)–(*b*) at the time step $t = 3820\,\mathrm{s}$ and (*c*)–(*d*) at time step $t = 3880\,\mathrm{s}$, before the $\mathbf{u}/p$ solution fails.

punch in an isothermal setting is given by [83]:

$$q = 4a\left(1 + \frac{\pi}{2}\right)\tau_{ps}$$

Table 3
Prandtl's Punch test: Peak load relative errors for the half-domain in an isothermal setting at 20 °C.

	Peak load [N]	Error [%]
$\mathbf{u}\mathbf{e}/p$	15,257	2.79
$\mathbf{u}/p$	15,264	2.84

where τ_{ps} is the yield stress threshold in pure shear, defined as a function the uniaxial yield stress threshold, σ_y, as $\tau_{ps} = \frac{\sigma_y}{\sqrt{3}}$ and $2a$ is the width of the punch ($2a = 1\,[\mathrm{m}]$). For a stress threshold $\sigma_y\,(20\,^\circ\mathrm{C}) = 10$ [kPa], the peak load for the half-domain is $q_{1/2} = 14,842.5\,[\mathrm{N/m}]$.

Table 3 presents the peak load for the isothermal setting of the half-domain computed by both FE formulations.

5.4.1. Case 1: Numerical simulation with null thermal conductivity

The objective of this simulation is to illustrate a case where the temperature increase is produced exclusively by the mechanical dissipation. The thermal conductivity is set to *zero* to emulate null thermal inertia. In this way, mechanical dissipation increases the temperature locally, without thermal conduction. Point *A*, shown in Fig. 24, is chosen to evaluate the evolution of the J2-stresses and the temperature, presented in Fig. 27. The $\mathbf{u}/p$ element produces a higher mechanical dissipation [35], resulting in a higher temperature increase, Fig. 27*a*, affecting the computed yield threshold and reducing the J2-stresses observed at point *A*, Fig. 27*b*.

In the isothermal setting, both mixed formulations reach the yield threshold value, $\sigma_y\,(20\,^\circ\mathrm{C}) = 10$ [kPa], for point *A*. On the other hand, the peak J2-stress values reached in the non-isothermal analysis are $\sigma_y = 9.51$ [kPa] and $\sigma_y = 8.94$ [kPa] for the mixed 3-field and $\mathbf{u}/p$ formulations, respectively. The J2-stresses decrease until they reach the final value of $\sigma_y = 6.95$ [kPa] and $\sigma_y = 6.65$ [kPa] for the 3-field and $\mathbf{u}/p$, respectively.

Fig. 28 shows snapshots of the failure mechanism (*a*–*b* — near the peak load; *c*–*d* at the final step) for both formulations. Although the failure mechanisms in both cases are similar, the $\mathbf{u}/p$ formulation shows some mesh sensitivity and presents a vertical slip line that does not develop in the 3-field.

5.4.2. Case 2: Numerical simulation with an external heat source

The following case introduces an external heat source in the problem and the thermal conductivity of the domain is set to $2.5 \cdot 10^{-3}\,[\mathrm{W/(m°C)}]$. The resulting effects on the failure mechanism,

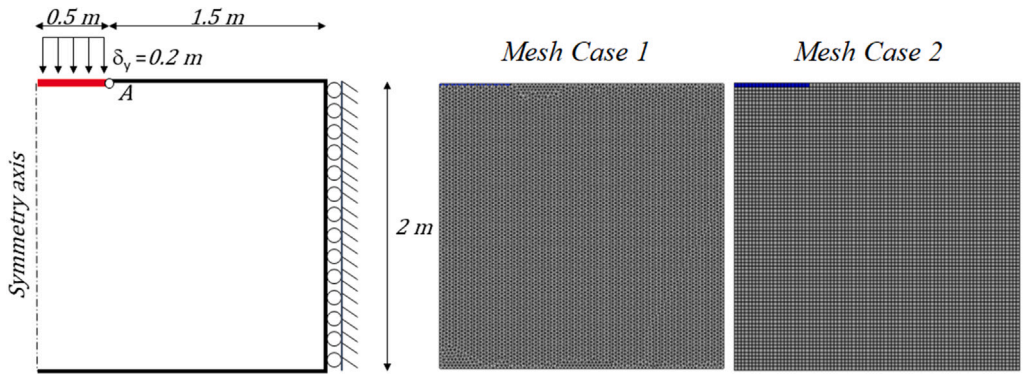

Fig. 24. Prandtl's Punch test: General problem setting and meshes.

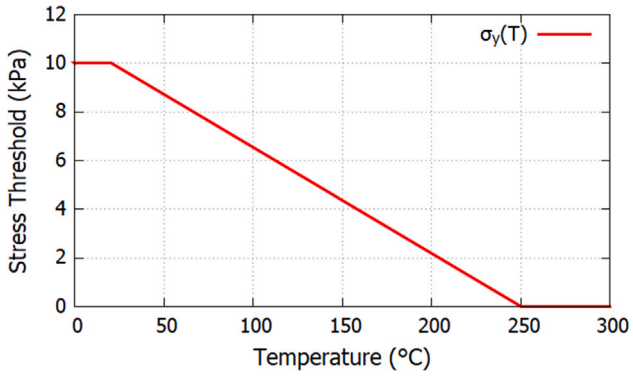

Fig. 25. Prandtl's Punch test: Temperature-dependency of the uniaxial stress threshold.

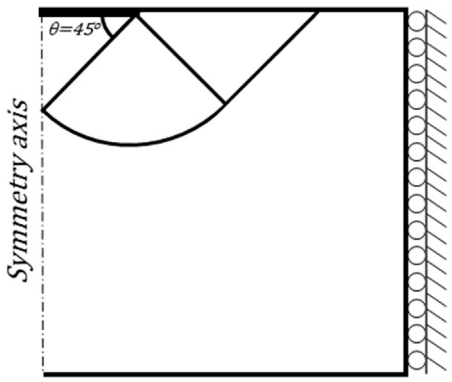

Fig. 26. Prandtl's Punch test: Collapse mechanism in an isothermal setting.

peak load and bearing capacity are explored. The heat source is positioned in the rigid punching area at a constant temperature of 150 [°C].

Fig. 29 shows snapshots of the failure mechanism (*a–b* — near the peak load; *c–d* — at the final step) for both formulations. The increase of temperature in the rigid footing area changes the failure mechanism with respect to the isothermal case, altering its depth, which eventually emerges closer to the heated area. Note that, due to the effect of temperature, the failure mechanism does no longer present a critical angle θ of 45°. Fig. 30(*a*) shows the difference in terms of strains between the computations of both formulations at the end of the simulation. Note that the difference is computed as $[\mathbf{u}/\mathbf{e}/p - \mathbf{u}/p]$, where *blue* values mean that the $\mathbf{u}/p$ solution has higher strains and *red* values otherwise. This represents the superposition of the $\mathbf{u}/p$ and $\mathbf{u}/\mathbf{e}/p$ mechanisms in *blue* and *red*, respectively. It can be seen how the two formulations do not produce the same results due to the poor precision of the $\mathbf{u}/p$ element. Fig. 30(*b*) shows the reaction vs displacement curves, where the effect of the thermal softening induced by the temperature-dependency of the yield stresses, as defined in Fig. 25, can be observed for both formulations. The reference curves are obtained from simulations without a temperature-dependent yield threshold. The higher peak-load observed in the 3-field is a consequence of the broader confined region below the rigid footing compared to the $\mathbf{u}/p$ formulation.

Table 4
Prandtl's Punch test — case 2: Difference between isothermal and non-isothermal critical angles on the slip-line and computed peak-load in the non-isothermal case.

Case	$\Delta\theta$	q [N]
$\mathbf{u}/p$	−13.24°	10,472
$\mathbf{u}/\mathbf{e}/p$	−7.69°	11,070

Table 4 shows the change in the critical angles with respect to the reference case ($\theta = 45°$) caused by the increase of temperature on the rigid footing. It also presents the reduced peak loads which are to be compared to the isothermal simulation results presented in Table 3.

Note that the 3-field formulation is able to produce the original Prandtl collapse mechanism (a slip-line), while the mixed $\mathbf{u}/p$ introduces a vertical punching line to the slip-line mechanism in both sets analyzed.

5.5. Singly perforated thin-walled cylinder

The next example is a thin-walled cylinder 0.6 [m] × 3 [m] × 0.02 [m] (*outer diameter* × *height* × *thickness*) with a perforation of 0.04 [m] × 0.04 [m] × 0.02 [m] (*width* × *height* × *thickness*) subjected to vertical stretching. The cylinder is heated at the perforation, as shown in Fig. 31, in an area of dimensions 0.12 [m] × 0.12 [m] × 0.02 [m] (*width* × *height* × *thickness*). The heat load is described in Fig. 32(*a*).

The constitutive model adopted is the J2-Damage with softening and the material properties are presented in Table 5. One fourth of the domain is considered due to the double symmetry of the problem (see Fig. 31).

As shown in Fig. 31, the perforated cylinder is in a state of plane stress, as the normal stress through the thickness is null. An imposed vertical displacement of $\delta_z = 0.20$ [m] is applied at the top boundary.

The yield stress threshold, σ_y, is temperature-dependent as shown in Fig. 32(*b*), following the observations in Ref. [82].

Fig. 31 presents the cylinder geometry and the structured mesh of hexahedral finite elements of size $h = 0.02$ [m] employed in the simulation, resulting in a total of 3749 elements.

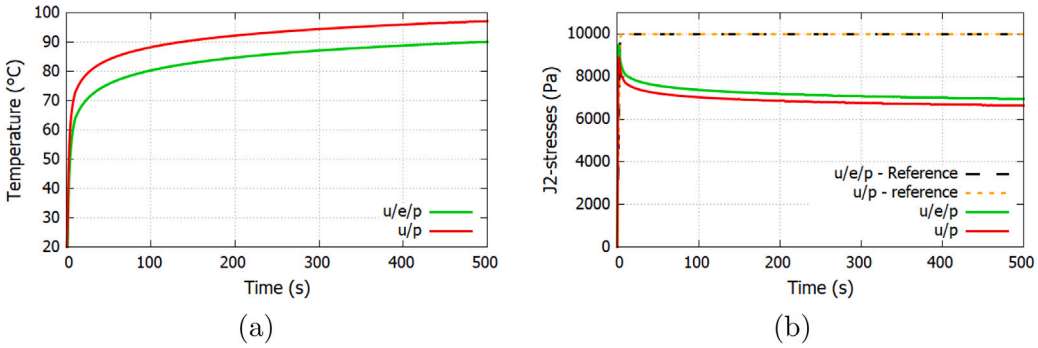

Fig. 27. Prandtl's Punch test — case 1: (*a*) Comparative evolution of the temperature and (*b*) J2-stresses at point *A*.

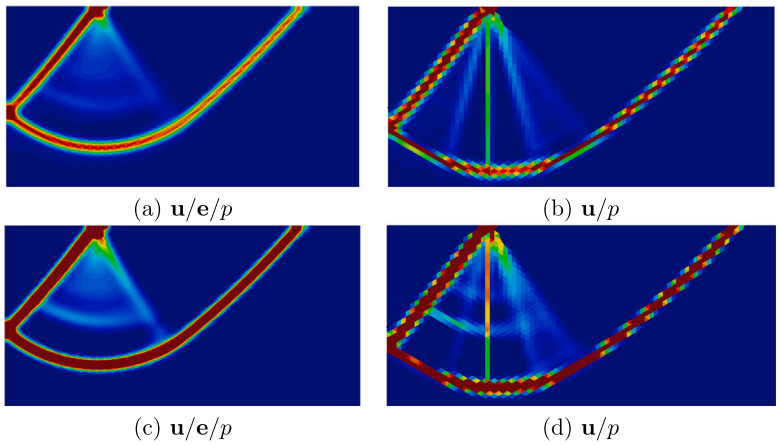

Fig. 28. Prandtl's Punch test — case 1: Collapse mechanisms (*a*)–(*b*) at $d_y = 0.02\,[\mathrm{m}]$ and (*c*)–(*d*) at $d_y = 0.20\,[\mathrm{m}]$.

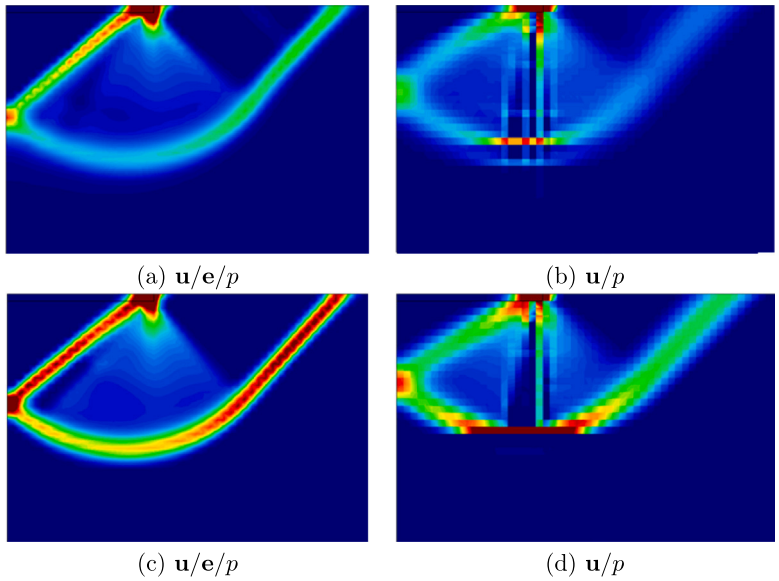

Fig. 29. Prandtl's Punch test — case 2: Collapse mechanisms (*a*)–(*b*) at $d_y = 0.02\,[\mathrm{m}]$ and (*c*)–(*d*) at $d_y = 0.20\,[\mathrm{m}]$.

Fig. 33 shows the load vs displacement curves of the singly perforated thin-walled cylinder computed for both formulations. It can be observed that the peak loads computed with both formulations are in good agreement in this case. However, an important difference on the mechanical dissipation can be appreciated in the analysis. This is caused by the poor evaluation of the stress field in the $\mathbf{u}/p$ formulation, which, as shown in Ref. [35] specially pollutes the computations in the nonlinear range. Conversely, the enhanced precision of the 3-field formulation allows to increase the accuracy of the discrete solution in

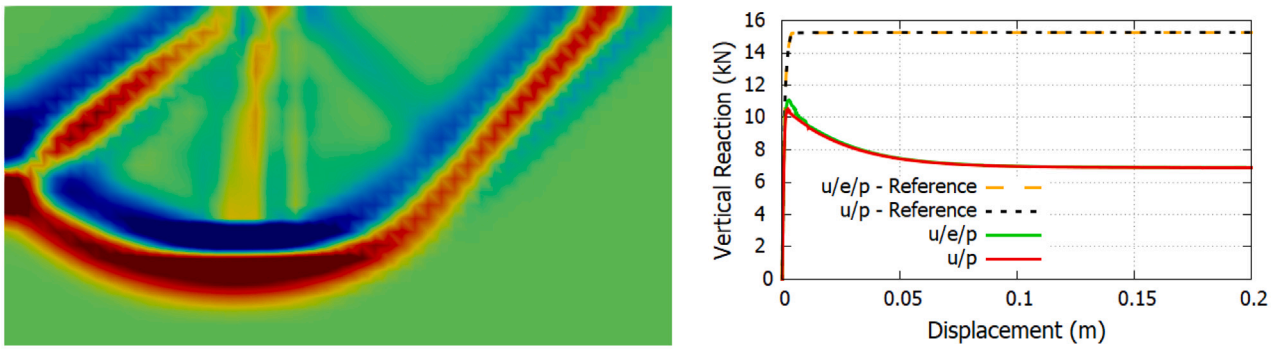

Fig. 30. Prandtl's Punch test — case 2: (*a*) Superimposed collapse mechanisms at $d_y = 0.20\,[\mathrm{m}]$. In *red* the $\mathbf{u}/\mathbf{e}/p$ solution and the $\mathbf{u}/p$ in *blue*; (*b*) Reaction vs displacement curves. (For interpretation of the references to colour in this figure legend, the reader is referred to the web version of this article.)

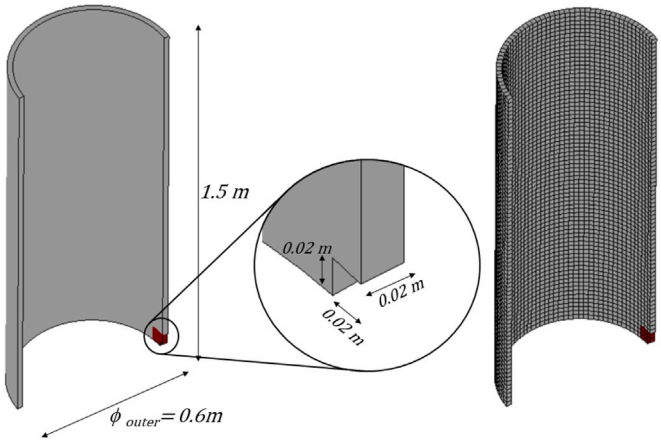

Fig. 31. Singly perforated thin-walled cylinder: Problem setting. Heated area in red. (For interpretation of the references to colour in this figure legend, the reader is referred to the web version of this article.)

Table 5
Singly perforated thin-walled cylinder: Material properties.

Property	Value
Young's Modulus [GPa]	200
Fracture Energy [MJ/m^2]	20
Density [kg/m^3]	7800
Thermal Conductivity [W/(m °C)]	45
Specific Heat Capacity [J/(kg °C)]	500

terms of stress and produces more reliable results, which is particularly crucial in nonlinear problems [35].

Fig. 34 shows the J2-strains at the mid-simulation, Fig. 34(*a*)–(*b*), and at the end of the simulation, Fig. 34(*c*)–(*d*). The difference in the evaluation of the stress field by both formulations produces the contrast observed in Fig. 34. The banding phenomenon, reported in Section 5.2 and in the work [27], is again observed in Fig. 34 for the $\mathbf{u}/p$ formulation when softening behavior is introduced, this time in a thermo-mechanical analysis, while the 3-field solution is correctly localizing in a continuous shear band. Fig. 35 exhibits the principal stress vectors for the same time-steps. There it can be seen the stress-locking phenomenon taking place in the $\mathbf{u}/p$ formulation, where stresses spuriously concentrate in the region of the shear band.

Fig. 36 shows the computed temperature field with both formulations at the time step $t = 750\,[\mathrm{s}]$. It can be seen that the temperature is higher in the area where the crack develops in the $\mathbf{u}/p$ solution as a result of the higher dissipation of this FE formulation. This evidences the over-dissipation due to stress locking, noticed in Figs. 33 and 35, that takes place in the $\mathbf{u}/p$ formulation due to lack of stress accuracy.

6. Conclusions

In this work, the numerical simulation of thermally-induced structural failure under incompressible conditions is addressed. For this, an enhanced accuracy $\mathbf{u}/\mathbf{e}/p$ formulation is employed and its performance is assessed against the classical $\mathbf{u}/p$ formulation. J2-damage and J2-plasticity nonlinear constitutive laws are introduced to represent the degradation of the isochoric material. Thermal coupling is introduced in the model following a staggered procedure.

The computation of several nonlinear benchmark applications is performed, including strain localization, plasticity and softening behavior. Temperature-dependent material properties are introduced and the influence of the temperature in structural failure is examined with respect to reference isothermal analyses.

It is observed that:

- The standard displacement-based FE formulation from solid mechanics cannot be used to compute problems including incompressible nonlinear constitutive behavior such as the Von Mises yield criterion.
- The 3-field and $\mathbf{u}/p$ FE formulations are both able of considering the elastic incompressibility and the isochoric deformations of the J2-plasticity and J2-damage constitutive models.
- The proposed 3-field FE has a much better performance compared with the $\mathbf{u}/p$ FE in terms of failure mechanisms, bearing capacity, mechanical dissipations, solution stability and is free of stress locking. These aspects are a consequence of the enhanced accuracy of the stress/strain fields considered. Correspondingly, the results computed with the $\mathbf{u}/p$ formulation present serious numerical difficulties in nonlinear applications.
- No spurious mesh dependency can be appreciated in the solutions computed with the $\mathbf{u}/\mathbf{e}/p$ element.
- The proposed method is able to solve incompressible problems using different FE meshes including triangles, quadrilaterals, hexahedra, etc.
- The model reproduces the theoretical load carrying capacity of the numerical benchmarks with accuracy.
- The coupling of the mixed 3-field FE for mechanical problems with the thermal problem is successful and many of the strong points of the 3-field formulation are inherited in thermo-mechanical applications.

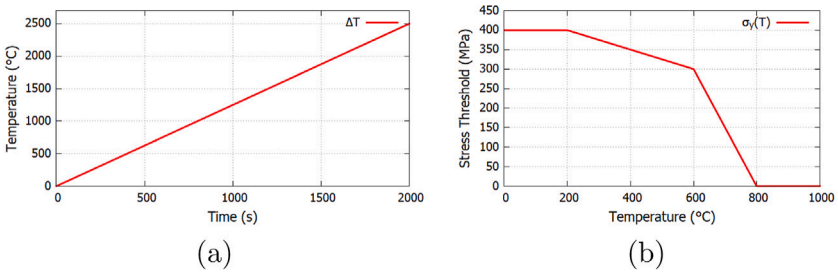

Fig. 32. Singly perforated thin-walled cylinder: (*a*) Temperature increase curve applied on the perforation and (*b*) the uniaxial yield stress threshold evolution with the temperature.

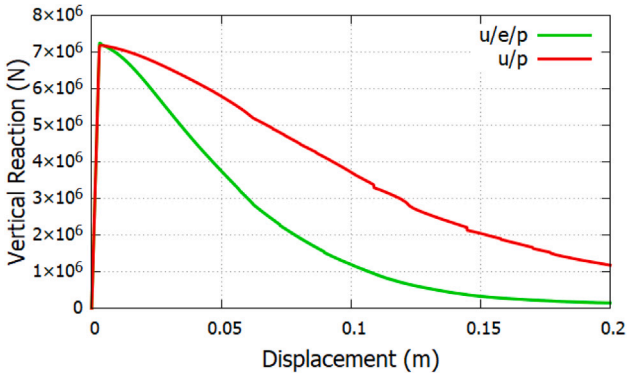

Fig. 33. Singly perforated thin-walled cylinder: Load vs displacement curve.

CRediT authorship contribution statement

Carlos A. Moreira: Formal analysis, Writing – original draft. **Gabriel B. Barbat:** Formal analysis, Writing – original draft. **Miguel Cervera:** Conceptualization, Writing – review & editing, Supervision. **Michele Chiumenti:** Writing – review & editing, Supervision.

Declaration of competing interest

The authors declare that they have no known competing financial interests or personal relationships that could have appeared to influence the work reported in this paper.

Acknowledgments

The authors gratefully acknowledge the financial support from the Spanish Ministry of Economy and Competitiveness, through the Severo Ochoa Programme for Centres of Excellence in R&D (CEX2018-000797-S).

This work has been supported by the European Union's horizon 2020 research and innovation programme (H2020-DT-2019-1 No. 872570) under the KYKLOS 4.0 Project (An Advanced Circular and Agile Manufacturing Ecosystem based on rapid reconfigurable manufacturing process and individualized consumer preferences) and by the Ministry of Science, Innovation and Universities (MCIU), Spain via: the PriMuS project (Printing pattern based and MultiScale enhanced performance analysis of advanced Additive Manufacturing components, ref. num. PID2020-115575RB-I00).

Appendix

The discrete virtual displacements, virtual deviatoric-strains and virtual pressure are approximated as:

$$\begin{aligned}\delta\mathbf{u} \doteq \delta\hat{\mathbf{u}} &= \delta\mathbf{u}_h + \delta\tilde{\mathbf{u}}\\ \delta\mathbf{e} \doteq \delta\hat{\mathbf{e}} &= \delta\mathbf{e}_h + \delta\tilde{\mathbf{e}}\\ \delta p \doteq \delta\hat{p} &= \delta p_h + \delta\tilde{p}\end{aligned} \tag{A.1}$$

Introducing these approximations and the ones in Eq. (42) into the continuous weak form in Eq. (30) and separating the FE and sub-grid scale terms results in the following system of equations:

$$\begin{aligned}
&\int_\Omega [\mathbf{S}\delta\mathbf{u}_h]^T(\mathbf{C}^{dev}\mathbf{e}_h)d\Omega + \int_\Omega [\mathbf{S}\delta\mathbf{u}_h]^T(\mathbf{C}^{dev}\tilde{\mathbf{e}})d\Omega\\
&+ \int_\Omega [\mathbf{S}\delta\mathbf{u}_h]^T(p_h\mathbf{I})d\Omega +\\
&+ \int_\Omega [\mathbf{S}\delta\mathbf{u}_h]^T(\tilde{p}\mathbf{I})d\Omega = W(\delta\mathbf{u}_h) \qquad \forall\delta\mathbf{u}_h \quad (a)\\
&\int_\Omega \delta\mathbf{e}_h^T[\mathbf{C}^{dev}\mathbf{S}\mathbf{u}_h]d\Omega + \int_\Omega \delta\mathbf{e}_h^T[\mathbf{C}^{dev}\mathbf{S}\tilde{\mathbf{u}}]d\Omega +\\
&- \int_\Omega \delta\mathbf{e}_h^T\mathbf{C}^{dev}\mathbf{e}_h d\Omega - \int_\Omega \delta\mathbf{e}_h^T\mathbf{C}^{dev}\tilde{\mathbf{e}}d\Omega = \mathbf{0} \qquad \forall\delta\mathbf{e}_h \quad (b)\\
&\int_\Omega \delta p_h^T(\mathbf{G}^T\mathbf{u}_h)d\Omega + \int_\Omega \delta p_h^T(\mathbf{G}^T\tilde{\mathbf{u}})d\Omega - \int_\Omega \delta p_h^T\tfrac{p_h}{C^{vol}}d\Omega\\
&- \int_\Omega \delta p_h^T\tfrac{\tilde{p}}{C^{vol}}d\Omega = 0 \qquad \forall\delta p_h \quad (c)\\
&\int_\Omega [\mathbf{S}\delta\tilde{\mathbf{u}}]^T(\mathbf{C}^{dev}\mathbf{e}_h)d\Omega + \int_\Omega [\mathbf{S}\delta\tilde{\mathbf{u}}]^T(\mathbf{C}^{dev}\tilde{\mathbf{e}})d\Omega\\
&+ \int_\Omega [\mathbf{S}\delta\tilde{\mathbf{u}}]^T(p_h\mathbf{I})d\Omega +\\
&+ \int_\Omega [\mathbf{S}\delta\tilde{\mathbf{u}}]^T(\tilde{p}\mathbf{I})d\Omega = W(\delta\tilde{\mathbf{u}}) \qquad \forall\delta\tilde{\mathbf{u}} \quad (d)\\
&\int_\Omega \delta\tilde{\mathbf{e}}^T[\mathbf{C}^{dev}\mathbf{S}\mathbf{u}_h]d\Omega + \int_\Omega \delta\tilde{\mathbf{e}}^T[\mathbf{C}^{dev}\mathbf{S}\tilde{\mathbf{u}}]d\Omega +\\
&- \int_\Omega \delta\tilde{\mathbf{e}}^T\mathbf{C}^{dev}\mathbf{e}_h d\Omega - \int_\Omega^T \delta\tilde{\mathbf{e}}^T\mathbf{C}^{dev}\tilde{\mathbf{e}}d\Omega = \mathbf{0} \qquad \forall\delta\tilde{\mathbf{e}} \quad (e)\\
&\int_\Omega \delta\tilde{p}^T(\mathbf{G}^T\mathbf{u}_h)d\Omega + \int_\Omega \delta\tilde{p}^T(\mathbf{G}^T\tilde{\mathbf{u}})d\Omega - \int_\Omega \delta\tilde{p}^T\tfrac{p_h}{C^{vol}}d\Omega\\
&- \int_\Omega \delta\tilde{p}^T\tfrac{\tilde{p}}{C^{vol}}d\Omega = 0 \qquad \forall\delta\tilde{p} \quad (f)
\end{aligned} \tag{A.2}$$

The system formed by the sub-grid scale Eqs. (A.2)*d*, (A.2)*e* and (A.2)*f* admits the following solution, corresponding to the residual based sub-grid approach,

$$\begin{aligned}\tilde{\mathbf{u}} &= \tau_u[\mathbf{S}^T(\mathbf{C}^{dev}\mathbf{e}_h) + \mathbf{G}p_h + \mathbf{f}]\\ \tilde{\mathbf{e}} &= \tau_e[\mathbf{W}\mathbf{u}_h - \mathbf{e}_h]\\ \tilde{p} &= \tau_p[\mathbf{G}^T\mathbf{u}_h - \tfrac{p_h}{C^{vol}}]\end{aligned} \tag{A.3}$$

where the stabilization parameters τ_u, τ_e and τ_p are chosen to obtain optimum convergence rates upon mesh refinement [71,84] as:

$$\begin{aligned}\tau_u &= \tfrac{c_u h L_0}{2\tilde{C}^{dev}}\\ \tau_e &= c_e\tfrac{h}{L_0}\\ \tau_p &= c_p\tilde{C}^{vol}\tfrac{h}{L_0}\end{aligned} \tag{A.4}$$

where L_0 is a characteristic length of the problem, c_u, c_e and c_p are arbitrary stabilization constants, h is the FE size and $\tilde{C}^{dev}$ is the secant shear modulus defined as

$$\tilde{C}^{dev} = \frac{\|\mathbf{s}_h\|}{2\|\mathbf{e}_h\|} \tag{A.5}$$

and $\tilde{C}^{vol}$ is the compressibility modulus obtained according to a Fourier analysis in [84] and defined as:

$$\tilde{C}^{vol} = \left(\frac{c_1}{2\tilde{G}} + \frac{c_2}{\tilde{K}}\right)^{-1} \tag{A.6}$$

where $\tilde{G}$ and $\tilde{K}$ are the *effective secant shear modulus* and *effective bulk modulus*, respectively. Choosing the constants $c_1 = 1$ and $c_2 = \frac{2}{3}$, and rewriting $\tilde{C}^{vol}$ in terms of $\tilde{G}$ leads to

$$\tilde{C}^{vol} = \frac{2}{3}\tilde{G}\left(\frac{1+\nu}{1-\nu}\right) \tag{A.7}$$

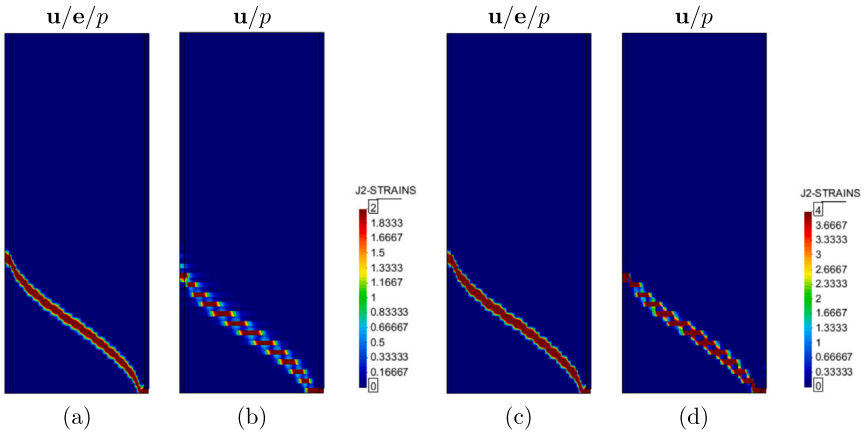

Fig. 34. Singly perforated thin-walled cylinder: J2-strains (*a*)–(*b*) at the mid-simulation and (*c*)–(*d*) at the final time step.

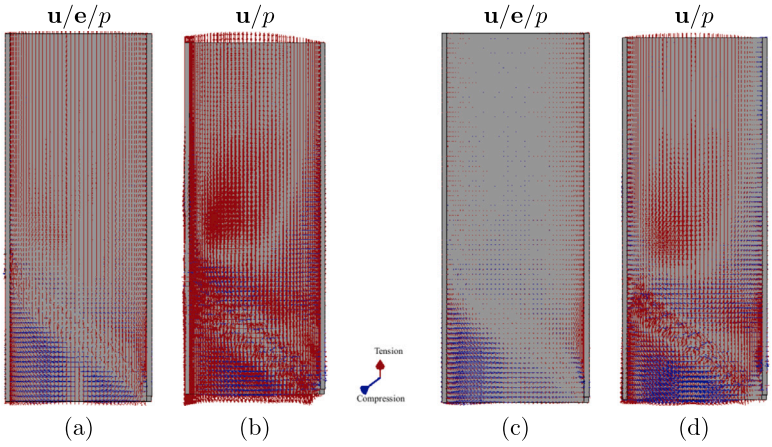

Fig. 35. Singly perforated thin-walled cylinder: Principal stresses vectors (*a*)–(*b*) at the mid-simulation and (*c*)–(*d*) at the final time step.

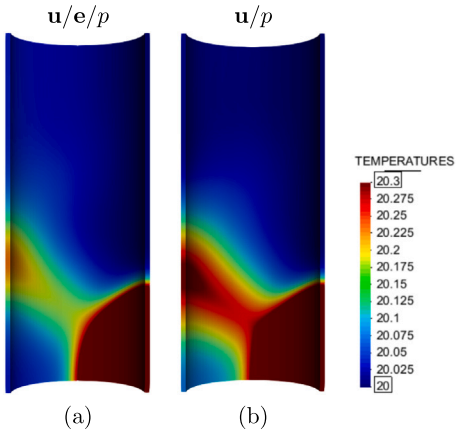

Fig. 36. Singly perforated thin-walled cylinder: Temperature field in [°C] computed with both formulations at the time step $t = 750$ [s].

Then $\tilde{\mathbf{u}}$, $\tilde{\mathbf{e}}$ and $\tilde{p}$ of Eq. (A.3) are introduced into the remaining equations (A.2)*a*, (A.2)*b* and (A.2)*c* to stabilize the discrete FE problem. Note that the stabilization terms in Eq. (A.3) tend to zero upon convergence as they correspond to the residual of the strong form of the problem.

With some manipulation, the stabilized weak form of the problem results in:

$$
\begin{aligned}
&(1-\tau_e)\int_\Omega [\mathbf{S}\delta\mathbf{u}_h]^T(\mathbf{C}^{dev}\mathbf{e}_h)d\Omega + \tau_e\int_\Omega [\mathbf{S}\delta\mathbf{u}_h]^T(\mathbf{C}^{dev}\mathbf{S}\mathbf{u}_h)d\Omega \\
&+(1-\tfrac{\tau_p}{C^{vol}})\int_\Omega [\mathbf{S}\delta\mathbf{u}_h]^T(p_h\mathbf{I})d\Omega \qquad \forall\delta\mathbf{u}_h \\
&+\tau_p\int_\Omega [\mathbf{S}\delta\mathbf{u}_h]^T(\mathbf{G}^T\mathbf{u}_h\mathbf{I})d\Omega = W(\delta\mathbf{u}_h) \\
&(1-\tau_e)\int_\Omega \delta\mathbf{e}_h^T[\mathbf{C}^{dev}\mathbf{S}\mathbf{u}_h]d\Omega \\
&-\tau_u\int_\Omega(\delta\mathbf{e}_h^T\mathbf{S}\mathbf{C}^{dev})(\mathbf{C}^{dev}\mathbf{S}^T\mathbf{e}_h)d\Omega+ \qquad \forall\delta\mathbf{e}_h \\
&-\tau_u\int_\Omega(\delta\mathbf{e}_h^T\mathbf{S})[\mathbf{C}^{dev}\mathbf{G}p_h]d\Omega \\
&-(1-\tau_e)\int_\Omega \delta\mathbf{e}_h^T\mathbf{C}^{dev}\mathbf{e}_h d\Omega = \mathbf{0} \\
&(1-\tfrac{\tau_p}{C^{vol}})\int_\Omega \delta p_h^T(\mathbf{G}^T\mathbf{u}_h)d\Omega - \tau_u\int_\Omega(\delta p_h^T\mathbf{G}^T)(\mathbf{C}^{dev}\mathbf{S}^T\mathbf{e}_h)d\Omega \\
&-\tau_u\int_\Omega(\delta p_h^T\mathbf{G}^T)(\mathbf{G}p_h)d\Omega+ \qquad \forall\delta p_h \\
&-(1-\tfrac{\tau_p}{C^{vol}})\int_\Omega \delta p_h^T\tfrac{p_h}{C^{vol}}d\Omega = 0
\end{aligned}
\tag{A.8}
$$

where the divergence theorem has been applied to the second and third terms of Eq. (A.8)*b* and (A.8)*c*. Note that in this process, the boundary terms of the sub-grid scales are neglected with respect to the other terms. In addition, the body forces, $\mathbf{f}$, are considered constant inside each element.

Next, the FE discrete form of the problem is obtained by substituting $\mathbf{u}_h$, $\mathbf{e}_h$ and p_h (and $\delta\mathbf{u}_h$, $\delta\mathbf{e}_h$, δp_h) by their FE discrete approximations:

$$
\begin{aligned}
&(1-\tau_e)\int_\Omega(\delta\mathbf{U}^T\underbrace{\mathbf{N}_u^T\mathbf{S}^T}_{=\mathbf{B}_u^T})(\mathbf{C}^{dev}\mathbf{N}_e\mathbf{E})d\Omega\\
&+\tau_e\int_\Omega(\delta\mathbf{U}^T\underbrace{\mathbf{N}_u^T\mathbf{S}^T}_{=\mathbf{B}_u^T})(\mathbf{C}^{dev}\underbrace{\mathbf{S}\mathbf{N}_u}_{=\mathbf{B}_u}\mathbf{U})d\Omega+ \qquad \forall\delta\mathbf{U}\\
&+(1-\tfrac{\tau_p}{C^{vol}})\int_\Omega\delta\mathbf{U}^T\mathbf{N}_u^T\mathbf{G}\mathbf{N}_p\mathbf{P}d\Omega\\
&+\tau_p\int_\Omega\delta\mathbf{U}^T\mathbf{N}_u^T\underbrace{\mathbf{S}^T\mathbf{I}}_{=\mathbf{G}}\mathbf{G}^T\mathbf{N}_u\mathbf{U}d\Omega=\quad\hat{W}(\delta\mathbf{U})\\
&(1-\tau_e)\int_\Omega\delta\mathbf{E}^T\mathbf{N}_e^T[\mathbf{C}^{dev}(\underbrace{\mathbf{S}\mathbf{N}_u}_{=\mathbf{B}_u}\mathbf{U})]d\Omega\\
&-\tau_u\int_\Omega(\delta\mathbf{E}^T\mathbf{N}_e^T\mathbf{S}\mathbf{C}^{dev})(\mathbf{C}^{dev}\mathbf{S}^T\mathbf{N}_e\mathbf{E})d\Omega \qquad \forall\delta\mathbf{E}\\
&-\tau_u\int_\Omega(\delta\mathbf{E}^T\mathbf{N}_e^T\mathbf{S})[\mathbf{C}^{dev}(\mathbf{G}\mathbf{N}_p\mathbf{P})]d\Omega\\
&-(1-\tau_e)\int_\Omega\delta\mathbf{E}^T\mathbf{N}_e^T\mathbf{C}^{dev}\mathbf{N}_e\mathbf{E}d\Omega=\mathbf{0}\\
&(1-\tfrac{\tau_p}{C^{vol}})\int_\Omega\delta\mathbf{P}^T\mathbf{N}_p^T(\mathbf{G}^T\mathbf{N}_u\mathbf{U})d\Omega\\
&-\tau_u\int_\Omega(\delta\mathbf{P}^T\mathbf{N}_p^T\mathbf{G}^T)(\mathbf{C}^{dev}\mathbf{S}^T\mathbf{N}_e\mathbf{E})d\Omega+ \qquad \forall\delta\mathbf{P}\\
&-\tau_u\int_\Omega(\delta\mathbf{P}^T\mathbf{N}_p^T\mathbf{G}^T)(\mathbf{G}\mathbf{N}_p\mathbf{P})d\Omega\\
&-(1-\tfrac{\tau_p}{C^{vol}})\int_\Omega\delta\mathbf{P}^T\mathbf{N}_p^T\tfrac{\mathbf{N}_p\mathbf{P}}{C^{vol}}d\Omega=0
\end{aligned}
\tag{A.9}
$$

with

$$
\hat{W}(\delta\mathbf{U})=\int_\Omega\delta\mathbf{U}^T\mathbf{N}_u^T\mathbf{f}d\Omega+\int_{\Gamma_t}\delta\mathbf{U}^T\mathbf{N}_u^T\bar{\mathbf{t}}d\Gamma \tag{A.10}
$$

Once again, the virtual displacement $\delta\mathbf{U}$, virtual deviatoric-strain $\delta\mathbf{E}$ and virtual pressure $\delta\mathbf{P}$ nodal vectors that appear in the system of Eqs. (A.9) are arbitrary, leading to the stabilized system of Eqs. (43).

References

[1] Zienkiewicz OC, Taylor LR, Zhu ZJ. The finite element method: Its basis and fundamentals. 6th ed. Butterworth-Heinemann; 2005.

[2] Miehe C. Aspects of the formulation and finite element implementation of large strain isotropic elasticity. Internat J Numer Methods Engrg 1994;37:1981–2004.

[3] Simo JC, Taylor RL, Pister KS. Variational and projection methods for the volume constraint in finite deformation elasto-plasticity. Comput Methods Appl Mech Engrg 1985;51:177–208.

[4] Simo JC, Rifai MS. A class of mixed assumed strain methods and the method of incompatible modes. Internat J Numer Methods Engrg 1990;29:1595–638.

[5] Agelet de Saracibar C, Chiumenti M, Valverde Q, Cervera M. On the orthogonal subgrid scale pressure stabilization of finite deformation J2 plasticity. Comput Methods Appl Mech Engrg 2006;195:1224–51.

[6] Arnold DN, Brezzi F, Fortin M. A stable finite element for the Stokes equations. Calcolo 1984;21:337–44.

[7] Arnold DN, Winther R. Mixed finite elements for elasticity. Numer Math 2002;92:401–19.

[8] Chama A, Reddy DB. New stable mixed finite element approximations for problems in linear elasticity. Comput Methods Appl Mech Engrg 2013;256:211–23.

[9] Malkus DS, Hughes TJR. Mixed finite element methods - reduced and selective integration techniques: A unification of concepts. Comput Methods Appl Mech Engrg 1978;15:63–81.

[10] Saloustros S, Cervera M, Kim S, Chiumenti M. Accurate and locking-free analysis of beams, plates and shells using solid elements. Comput Mech 2021. http://dx.doi.org/10.1007/s00466-020-01969-0.

[11] Cervera M, Chiumenti M, Di Capua D. Benchmarking on bifurcation and localization in J2 plasticity for plane stress and plane strain conditions. Comput Methods Appl Mech Engrg 2012;241–244:206–24.

[12] Baiocchi C, Brezzi F, Franca L. Virtual bubbles and Galerkin/least-squares type methods (Ga.L.S.). Comput Methods Appl Mech Engrg 1993;105:125–41.

[13] Kasper EP, Taylor RL. A mixed-enhanced strain method. I: Geometrically linear problems. II: Geometrically nonlinear problems. Comput Struct 2000;75:237–50, 251–260.

[14] Reddy BD, Simo JC. Stability and convergence of a class of enhanced assumed strain methods. SIAM J Numer Anal 1995;32:1705–28.

[15] Bonet J, Burton AJ. A simple average nodal pressure tetrahedral element for incompressible and nearly incompressible dynamic explicit applications. Commun Numer Methods Eng 1998;1(4):437–49.

[16] Bonet J, Marriot H, Hassan O. An averaged nodal deformation gradient linear tetrahedral element for large strain explicit dynamic applications. Commun Numer Methods Eng 2001;17:551–61.

[17] Bonet J, Marriot H, Hassan O. Stability and comparison of different linear tetrahedral formulations for nearly incompressible explicit dynamic applications. Internat J Numer Methods Engrg 2001;50:119–33.

[18] Dohrmann CR, Heinstein MW, Jung J, Key SW, Witkowsky WR. Node-based uniform strain elements for three-node triangular and four-node tetrahedral meshes. Internat J Numer Methods Engrg 2000;47:1549–68.

[19] de Souza Neto EA, Pires FMA, Owen DRJ. F-bar-based linear triangles and tetrahedra for finite strain analysis of nearly incompressible solids. Part I: Formulation and benchmarking. Internat J Numer Methods Engrg 2005;62:353–83.

[20] Hughes TJ. Generalization of selective integration procedures to anisotropic and nonlinear media. Internat J Numer Methods Engrg 1980;15(9):1413–8. http://dx.doi.org/10.1002/nme.1620150914.

[21] Nagtegaal JC, Parks DM, Rice JR. On numerically accurate finite element solutions in the fully plastic range. Comput Methods Appl Mech Engrg 1974;4(2):153–77. http://dx.doi.org/10.1016/0045-7825(74)90032-2.

[22] Sloan SW, Randolph MF. Numerical prediction of collapse loads using finite element methods. Int J Numer Anal Methods Geomech 1982;6(1):47–76. http://dx.doi.org/10.1002/nag.1610060105.

[23] Barbat GB, Cervera M, Chiumenti M. Appraisement of planar, bending and twisting cracks in 3D with isotropic and orthotropic damage models. Int J Fract 2018;210(1–2):45–79. http://dx.doi.org/10.1007/s10704-018-0261-3.

[24] Barbat GB, Cervera M, Chiumenti M. Structural size effect: Experimental, theoretical and accurate computational assessment. Eng Struct 2020;213:110555. http://dx.doi.org/10.1016/j.engstruct.2020.110555.

[25] Cervera M, Barbat GB, Chiumenti M. Finite element modelling of quasi-brittle cracks in 2D and 3D with enhanced strain accuracy. Comput Mech 2017;60(5):767–96. http://dx.doi.org/10.1007/s00466-017-1438-8.

[26] Cervera M, Barbat GB, Chiumenti M. Architecture of a multi-crack model with full closing, reopening and sliding capabilities. Comput Mech 2020;65:1593–620. http://dx.doi.org/10.1007/s00466-020-01836-y.

[27] Cervera M, Chiumenti M, Benedetti L, Codina R. Mixed stabilized finite element methods in nonlinear solid mechanics. Part III: Compressible and incompressible plasticity. Comput Methods Appl Mech Engrg 2015;285:752–75.

[28] Cervera M, Chiumenti M, Codina R. Mixed stabilized finite element methods in nonlinear solid mechanics. Part I: Formulation. Comput Methods Appl Mech Engrg 2010;199:2559–70.

[29] Cervera M, Chiumenti M, Codina R. Mixed stabilized finite element methods in nonlinear solid mechanics. Part II: Strain localization. Comput Methods Appl Mech Engrg 2010;199:2571–89.

[30] Cervera M, Chiumenti M, Codina R. Mesh objective modeling of cracks using continuous linear strain and displacement interpolations. Internat J Numer Methods Engrg 2011;87(10):962–87.

[31] Vlachakis G, Cervera M, Barbat GB, Saloustros S. Out-of-plane seismic response and failure mechanism of masonry structures using finite elements with enhanced strain accuracy. Eng Fail Anal 2019;97:534–55. http://dx.doi.org/10.1016/j.engfailanal.2019.01.017.

[32] Cervera M, Barbat GB, Chiumenti M, Wu J-Y. A comparative review of xfem, mixed fem and phase-field models for quasi-brittle cracking. Arch Computat Methods Eng 2022;29:1009–83. http://dx.doi.org/10.1007/s11831-021-09604-8.

[33] Castañar I, Baiges J, Codina R, Venghaus H. Topological derivative-based topology optimization of incompressible structures using mixed formulations. Comput Methods Appl Mech Engrg 2022;390:114438. http://dx.doi.org/10.1016/j.cma.2021.114438.

[34] Chiumenti M, Cervera M, Codina R. A mixed three-field FE formulation for stress accurate analysis including the incompressible limit. Comput Methods Appl Mech Engrg 2015;283:1095–116.

[35] Chiumenti M, Cervera M, Moreira CA, Barbat GB. Stress, strain and dissipation accurate 3-field formulation for inelastic isochoric deformation. Finite Elem Anal Des 2021;192:103534. http://dx.doi.org/10.1016/j.finel.2021.103534.

[36] Castañar I, Baiges J, Codina R. A stabilized mixed finite element approximation for incompressible finite strain solid dynamics using a total lagrangian formulation. Computer Methods in Applied Mechanics and Engineering 2020;368:113164. http://dx.doi.org/10.1016/j.cma.2020.113164.

[37] Cervera M, Chiumenti M. Size effect and localization in J_2 plasticity. Int J Solids Struct 2009;46:3301–12.

[38] Cervera M, Chiumenti M, Agelet de Saracibar C. Softening, localization and stabilization: Capture of discontinuous solutions in J2 plasticity. Int J Numer Anal Methods Geomech 2004;28:373–93.

[39] Cervera M, Chiumenti M, Agelet de Saracibar C. Shear band localization via local J_2 continuum damage mechanics. Comput Methods Appl Mech Engrg 2004;193:849–80.

[40] Chiumenti M, Valverde Q, Agelet de Saracibar C, Cervera M. A stabilized formulation for incompressible plasticity using linear triangles and tetrahedra. Int J Plast 2004;20:1487–504.

[41] Pastor M, Li T, Liu X, Zienkiewicz OC. Stabilized low-order finite elements for failure and localization problems in undrained soils and foundations. Comput Methods Appl Mech Engrg 1999;174:219–34.

[42] Bary B, Ranc G, Durand S, Carpentier O. A coupled thermo-hydro-mechanical-damage model for concrete subjected to moderate temperatures. Int J Heat Mass Transfer 2008;51:2847–62. http://dx.doi.org/10.1016/j.ijheatmasstransfer.2007.09.021.

[43] Li G, Cinefra M, Carrera E. Coupled thermo-mechanical finite element models with node-dependent kinematics for multi-layered shell structures. Int J Mech Sci 2020;171:105379. http://dx.doi.org/10.1016/j.ijmecsci.2019.105379.

[44] Sanavia L, Pesavento F, Schrefler BA. Finite element analysis of non-isothermal multiphase geomaterials with application to strain localization simulation. Comput Mech 2006;37:331. http://dx.doi.org/10.1007/s00466-005-0673-6.

[45] Wang K, Song X. Strain localization in non-isothermal unsaturated porous media considering material heterogeneity with stabilized mixed finite elements. Comput Methods Appl Mech Engrg 2020;359:112770. http://dx.doi.org/10.1016/j.cma.2019.112770.

[46] Carrera E, Cinefra M, Petrolo M, Zappino E. Finite element analysis of structures through unified formulation. In: Finite element analysis of structures through unified formulation. 2014, http://dx.doi.org/10.1002/9781118536643.

[47] Carrera E. Temperature profile influence on layered plates response considering classical and advanced theories. AIAA J 2002;40:1885–96. http://dx.doi.org/10.2514/2.1868.

[48] Carrera E. Transverse normal strain effect on thermal stress analysis of Homogeneous and layered plates. AIAA J 2005;43:2232–42. http://dx.doi.org/10.2514/1.11230.

[49] Robaldo A, Carrera E, Benjeddou A. Unified formulation for finite element thermoelastic analysis of multilayered anisotropic composite plates. J Therm Stresses 2005;28:1031–65. http://dx.doi.org/10.1080/01495730590964963.

[50] Carrera E, Boscolo M, Robaldo A. Hierarchic multilayered plate elements for coupled multifield problems of piezoelectric adaptive structures: Formulation and numerical assessment. Arch Comput Methods Eng 2007;14:383–430. http://dx.doi.org/10.1007/s11831-007-9012-8.

[51] Robaldo A, Carrera E, Benjeddou A. A unified formulation for finite element analysis of piezoelectric plates. Comput Struct 2006;84:1494–505. http://dx.doi.org/10.1016/j.compstruc.2006.01.029.

[52] Carrera E, Brischetto S, Nali P. Variational statements and computational models for MultiField problems and multilayered structures. Mech Adv Mater Struct 2008;15:182–98. http://dx.doi.org/10.1080/15376490801907657.

[53] Carrera E, Brischetto S, Fagiano C, Nali P. Mixed multilayered plate elements for coupled magneto-electro-elastic analysis. Multidiscip Model Mater Struct 2009;5:251–6. http://dx.doi.org/10.1163/157361109789017050.

[54] Carrera E, Fazzolari FA, Cinefra M. Thermal stress analysis of composite beams, plates and shells: Computational modelling and applications. Academic Press; 2015, p. 440.

[55] Gavagnin C, Sanavia L, De Lorenzis L. Stabilized mixed formulation for phase-field computation of deviatoric fracture in elastic and poroelastic materials. Comput Mech 2020;65:1447–65. http://dx.doi.org/10.1007/s00466-020-01829-x.

[56] Jha B, Juanes R. A locally conservative finite element framework for the simulation of coupled flow and reservoir geomechanics. Acta Geotech 2007;2:139–53. http://dx.doi.org/10.1007/s11440-007-0033-0.

[57] Lewis R, Schrefler B. Finite element method in the deformation and consolidation of porous media. New York: Wiley; 1998.

[58] White JA, Borja I. Stabilized low-order finite elements for coupled solid-deformation/fluid-diffusion and their application to fault zone transients. Comput Methods Appl Mech Engrg 2008;197:4353–66. http://dx.doi.org/10.1016/j.cma.2008.05.015.

[59] Babuska I. Error-bounds for finite element method. Numer Math 1971;16:322–33.

[60] Brezzi F, Fortin M. Mixed and hybrid finite element methods. New York: Springer; 1991.

[61] Codina R, Badia S, Baiges J, Principe J. Variational multiscale methods in computational fluid dynamics. In: Encyclopedia of computational mechanics. John Wiley & Sons, Ltd.; 2017, p. 1–28.

[62] Hughes TJR. Multiscale phenomena: Green's function, Dirichlet-to Neumann formulation, subgrid scale models, bubbles and the origins of stabilized formulations. Comput Methods Appl Mech Engrg 1995;127:387–401.

[63] Hughes TJR, Feijoó GR, L. Mazzei, Quincy JB. The variational multiscale method-a paradigm for computational mechanics, echanics. Comput Methods Appl Mech Engrg 1998;166:3–28.

[64] Badia S, Codina R. Stabilized continuous and discontinuous Galerkin techniques for Darcy flow. Comput Methods Appl Mech Engrg 2010;199:1654–67.

[65] Codina R. Stabilization of incompressibility and convection through orthogonal sub-scales in finite element methods. Comput Methods Appl Mech Engrg 2000;190:1579–99.

[66] Codina R. Finite element approximation of the three field formulation of the Stokes problem using arbitrary interpolations. SIAM J Numer Anal 2009;47:699–718.

[67] Cervera M, Chiumenti M, Valverde Q, Agelet de Saracibar C. Mixed linear/linear simplicial elements for incompressible elasticity and plasticity. Comput Methods Appl Mech Engrg 2003;192:5249–63.

[68] Chiumenti M, Valverde Q, Agelet de Saracibar C, Cervera M. A stabilized formulation for incompressible elasticity using linear displacement and pressure interpolations. Comput Methods Appl Mech Engrg 2002;191:5253–64.

[69] Codina R, Blasco J. Stabilized finite element method for transient Navier–Stokes equations based on pressure gradient projection. Comput Methods Appl Mech Engrg 2000;182:287–300.

[70] Codina R. Stabilized finite element approximation of transient incompressible flows using orthogonal subscales. Comput Methods Appl Mech Engrg 2002;191:4295–321.

[71] Castillo E, Codina R. Variational multi-scale stabilized formulations for the stationary three-field incompressible viscoelastic flow problem. Comput Methods Appl Mech Engrg 2014;279:579–605.

[72] Agelet De Saracibar C, Cervera M, Chiumenti M. On the formulation of coupled thermoplastic problems with phase-change. Int J Plast 1999;15(1):1–34.

[73] Agelet de Saracibar C, Cervera M, Chiumenti M. On the constitutive modeling of coupled thermomechanical phase-change problems. Int J Plast 2001;17(12):1565–622.

[74] Chiumenti M, Cervera M, Agelet de Saracibar C, Dialami N. Numerical modeling of friction stir welding processes. Comput Method Appl Mech Engrg 2013;254:353–69.

[75] Dialami N. Cervera M, Chiumenti M, Agelet de Saracibar C. Local–global strategy for the prediction of residual stresses in FSW processes. Int J Adv Manuf Technol 2017;88(3099):9–3111. http://dx.doi.org/10.1007/s00170-016-9016-3.

[76] Bazant ZP, Oh BH. Crack band theory for fracture of concrete. Mater Struct 1983;16:155–77.

[77] Pietruszczak S, Mroz Z. Finite element analysis of deformation of strain-softening materials. Internat J Numer Methods Engrg 1981;17:327–34.

[78] Cervera M, Agelet de Saracibar C, Chiumenti M. COMET: Coupled mechanical and thermal analysis. Data input manual, version 5.0. Technical report IT-308, 2002, http://www.cimne.upc.es.

[79] GiD v13 Reference Manual, Coll A, Ribó R, Pasenau M, Escolano E, Perez J Suit. CIMNE. CIMNE; 2016.

[80] Ahrens J, Geveci B, Law C. Paraview: An end-user tool for large data visualization, visualization handbook. Elsevier; 2005.

[81] Lubliner J. Plasticity theory. In: Dover books on engineering. Dover Publications; 2008.

[82] Bhatti Ayjwat A, Barsoum Zuheir, Murakawa Hidekazu, Barsoum Imad. Influence of thermo-mechanical material properties of different steel grades on welding residual stresses and angular distortion. Mater Des 2014;65:878–89. http://dx.doi.org/10.1016/j.matdes.2014.10.019.

[83] Hill R. The mathematical theory of plasticity. Oxford University Press; 1950.

[84] Badia S, Codina R. Unified stabilized finite element formulations for the Stokes and the Darcy problems. SIAM J Numer Anal 2009;17:309–30.